

Imaging the Néel vector switching in the monolayer antiferromagnet MnPSe_3 with strain-controlled Ising order

Zhuoliang Ni,¹ A. V. Haglund,² H. Wang,³ B. Xu,⁴ C. Bernhard,⁴ D. G. Mandrus,^{2,5} X. Qian,³ E. J. Mele,¹ C. L. Kane,¹ and Liang Wu^{1,*}

¹*Department of Physics and Astronomy, University of Pennsylvania, Philadelphia, Pennsylvania 19104, U.S.A*

²*Department of Materials Science and Engineering,
University of Tennessee, Knoxville, TN 37996, U.S.A.*

³*Department of Materials Science and Engineering,
Texas A&M University, College Station, TX 77843 U.S.A*

⁴*Department of Physics and Fribourg Center for Nanomaterials,
University of Fribourg, Chemin du Musée 3, CH-1700 Fribourg, Switzerland*

⁵*Materials Science and Technology Division, Oak Ridge National Laboratory, Oak Ridge, TN, 37831, U.S.A.*

(Dated: April 8, 2021)

The family of monolayer two-dimensional (2D) materials hosts a wide range of interesting phenomena, including superconductivity [1], charge density waves [2], topological states [3] and ferromagnetism [4], but direct evidence for antiferromagnetism in the monolayer has been lacking [5]. Nevertheless, antiferromagnets have attracted enormous interest recently in spintronics due to the absence of stray fields and their terahertz resonant frequency [6]. Despite the great advantages of antiferromagnetic spintronics, controlling and detecting Néel vectors have been limited in bulk materials [6–10]. In this work, we developed a sensitive second harmonic generation (SHG) microscope and detected long-range Néel antiferromagnetic (AFM) order and Néel vector switching down to the monolayer in MnPSe_3 . Temperature-dependent SHG measurement in repetitive thermal cooling surprisingly collapses into two curves, which correspond to the switching of an Ising type Néel vector reversed by the time-reversal operation, instead of a six-state clock ground state expected from the threefold rotation symmetry in the structure [11–13]. We imaged the spatial distribution of the Néel vectors across samples and rotated them by an arbitrary angle irrespective of the lattice in the sample plane by applying strain. By studying both a Landau theory and a microscopic model that couples strain to nearest-neighbor exchange, we conclude that the phase transition of the XY model in the presence of strain falls into the Ising universality class instead of the XY one, which could explain the extreme strain tunability. Finally, we found that the 180° AFM domain walls are highly mobile down to the monolayer after thermal cycles, paving the way for future control of the antiferromagnetic domains by strain or external fields

on demand for ultra-compact 2D AFM terahertz spintronics.

Detection and control of the spin order in ferromagnetic materials is the main principle in current information technology. The discovery of 2D ferromagnetic materials using the polar Kerr effect [4, 14] has triggered tremendous interest in studying magnetism in the true 2D limit [15–18] and spintronic device applications in van der Waals heterostructure materials [19–24]. Optical techniques are powerful tools to detect magnetism [5], but clear evidence for the AFM order in atomically thin 2D crystals has not been identified due to the lack of sensitive direct detection. The polar Kerr effect is absent in AFM materials when the total magnetization is zero [5, 25–27]. Although Raman spectroscopy is a powerful tool to study spin-phonon coupling and collective magnons [28–31], their identification often do not provide unambiguous identification of the AFM order [5, 32]. Non-optical methods such as tunneling magnetoresistance measurement have indicated the correlation in the monolayer of an AFM material [33], but it is also not a direct probe of the AFM order parameter [5, 32]. SHG has been shown to be a sensitive tool to detect AFM orders due to inversion symmetry breaking from the spin order in magneto-electric materials including bulk Cr_2O_3 [34], few-layer MnPSe_3 [35] and a synthetic bilayer CrI_3 [36]. Nevertheless, the detection of intrinsic AFM in the monolayer has not been demonstrated yet, which remains an unresolved fundamental question and is also not ideal for AFM terahertz spintronics at the smallest scales. In this work, we systematically study the layer-dependent AFM order, Néel vector distribution, switching and its strain tunability in a 2D crystal of MnPSe_3 [1] by a newly developed sensitive SHG imaging microscope. (See methods.)

MnPSe_3 belongs to the family of AFM transition metal phosphorous trichalcogenide MPX_3 ($\text{M} = \text{Mn, Ni, Fe, Co}$, $\text{X} = \text{S, Se}$), among which Mn compounds form inversion-breaking Néel order while others are in centrosymmetric Zigzag ordered phases [1, 38–42]. In contrast to MnPSe_3 , which has dominant out-of-plane moments [41, 43], MnPSe_3 has in-plane spins with very large

*Electronic address: liangwu@sas.upenn.edu

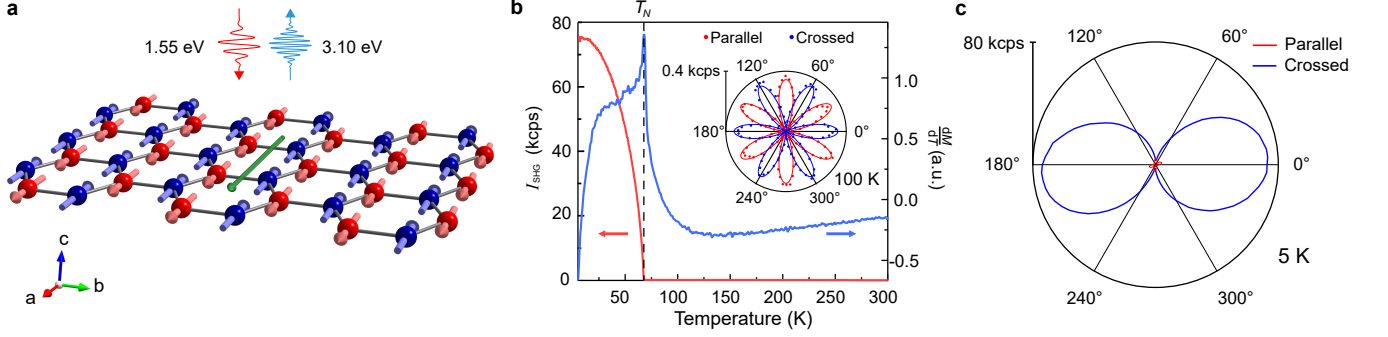


FIG. 1: **Characterization of bulk MnPSe₃ samples.** **a**, A schematic of the in-plane AFM Néel order and SHG measurement on MnPSe₃. The Mn atoms in each layer form a honeycomb lattice. The green arrow denotes the Néel vector. Laser pulses centered at 1.55 eV are normally incident on the *ab* plane and reflected light at the second-harmonic frequency is detected. **b**, Temperature dependence of SHG intensity (red) on a 100-nm sample exfoliated on SiO₂/Si and the temperature derivative of the in-plane magnetic susceptibility of a bulk crystal (blue). ‘kcps’ stands for one thousand counts per second. The transition temperature is marked by the black dashed line. Inset: Polarization-resolved EQ SHG of the 100-nm flake at 100 K. The dots are the data and the solid lines are the fits. **c**, Polarization-resolved SHG polar patterns of the same 100-nm thick MnPSe₃ flake measured at 5 K (All of the lines are experimental data). 0° is defined as the angle between the polarization of the incidence pulse and the horizontal direction in the lab.

XY anisotropy according to the neutron scattering measurement [1] (Fig. 1a), which offers richer magnetic domain structures such as vortices and tunability [13]. Above the Néel temperature, T_N , MnPSe₃ belongs to the point group $\bar{3}$ (S_6) and space group 148 [1], and has an inversion center between two neighboring Mn atoms but no mirror symmetry. The Mn atoms form a honeycomb lattice in one layer (Fig. 1a), and the honeycomb layers form the rhombohedral (ABC) stacking along the *c* axis with a threefold rotational symmetry. Different from FePS₃ and NiPS₃, which have a change of twofold rotational symmetry in the bulk to a threefold rotational symmetry in the monolayer [28, 29, 44, 45], MnPSe₃ is always three-fold symmetric. As shown in the inset of Fig. 1b, a small temperature-independent SHG from the electric quadrupole (EQ) contribution, $I_i^{EQ}(2\omega) \sim |\sum_{jkl} \chi_{ijkl}^{EQ} E_j(\omega) \nabla_k E_l(\omega)|^2$ follows the lattice threefold rotational symmetry above T_N . (See methods.) The parallel and crossed configuration correspond to $E(2\omega)/E(\omega)$ and $E(2\omega) \perp E(\omega)$ respectively while we co-rotate $E(\omega)$ and $E(2\omega)$ by 360° in the *ab* plane [46]. Below the Néel temperature, the formation of the Néel AFM order with in-plane spins breaks the inversion symmetry (\mathcal{P}), which allows electric dipole (ED) contribution to the SHG, $I_i^{ED}(2\omega) \sim |\sum_{jk} \chi_{ijk}^{ED}(\mathbf{L}) E_j(\omega) E_k(\omega)|^2$ [34]. $\chi_{ijk}^{ED}(\mathbf{L})$ is proportional to the order parameter, the Néel vector \mathbf{L} , [2] and changes the sign when \mathbf{L} flips by 180° ($\mathbf{L} = \mathbf{M}_1 - \mathbf{M}_2$, where \mathbf{M}_1 and \mathbf{M}_2 are the magnetization of two neighboring Mn atoms). (See Fig. 1a). In the AFM state, the product of the inversion symmetry (\mathcal{P}) and the time-reversal symmetry (\mathcal{T}), so called \mathcal{PT} symmetry, is still preserved [48], even though both \mathcal{P} and \mathcal{T} are broken. This kind of ED term is often called non-reciprocal or c-type SHG allowed by the \mathcal{PT} symmetry, while the EQ term is an i-type SHG, where ‘c’ and ‘i’

mean changing and invariant under time-reversal symmetry respectively [34]. Fig. 1b shows a typical SHG response as a function of temperature on a ~ 100 -nm thick flake exfoliated on SiO₂/Si. A sharp turn-on of the ED SHG signal clearly indicates a phase transition at 67.9 ± 0.2 K, agreeing well with the T_N (68 ± 0.5 K) determined from in-plane magnetization measurement. Below T_N , as shown in Fig. 1c, a giant twofold signal emerges in the crossed configuration, which clearly breaks the threefold rotation symmetry. Another surprising observation is that the peak of the parallel polar pattern is only 1/20 of that in the crossed pattern, which was not observed in previous \mathcal{PT} invariant van der Waals AFM materials [35, 36]. The nodal direction of the twofold crossed pattern is also shown to be close to the Néel vector direction (see Supplementary Note 1 and 2).

After confirming the detection of AFM order by SHG, we use scanning SHG microscopy with 2 μm spatial resolution to study the AFM domains. In MnPSe₃ with in-plane spins and large XY anisotropy [1, 43], six energetically equal magnetic domains are expected due to the threefold rotational crystalline anisotropy and the time-reversal operation [11–13]. Nevertheless, Fig. 2a shows that temperature-dependent SHG under ten consecutive cooling runs across T_N on the same spot of a 15- μm thick sample collapses onto two curves instead of six. The crossed and parallel polar patterns that respond to these two AFM domains are shown in Fig. 2b,c. To figure out the relation between these two domains, we performed spatial scanning SHG microscopy at 5 K with angles of the two polarizers chosen near the maximum signal in the crossed pattern. An optical image of a region with uniform thickness (~ 100 nm, a second exfoliated thick sample) and SHG maps at 5 K after two cooling processes across T_N are shown in Fig. 2d-f. Sharp dark lines with very low SHG intensity are observed, with bright domains

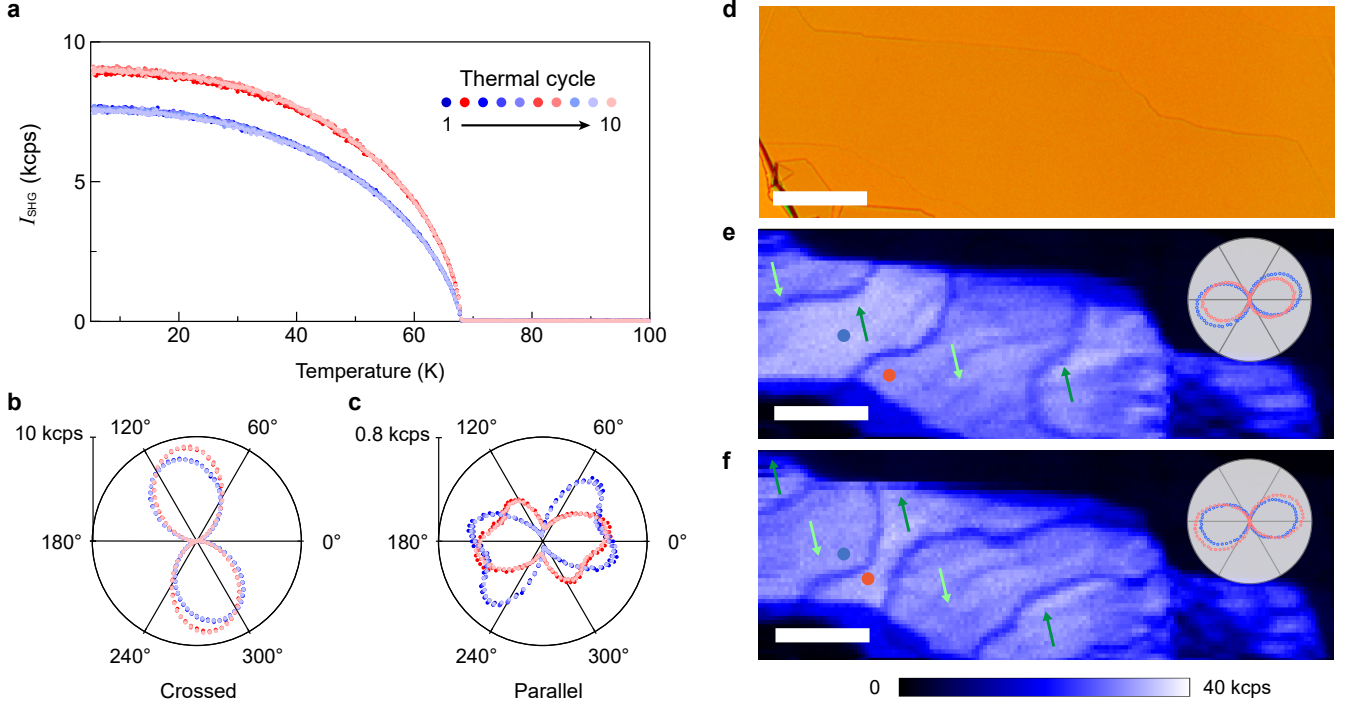


FIG. 2: **Ising-type Néel vector switching in MnPSe₃** **a**, Temperature-dependence of SHG intensity at the same spot on a $\sim 15\text{-}\mu\text{m}$ thick flake for 10 consecutive cooling runs across T_N . **b-c**, Polarization-dependent SHG patterns (**b**: crossed and **c**: parallel) measured at 5 K after each cooling in (**a**). **d**, An optical image of a thick MnPSe₃ flake ($\sim 100\text{ nm}$). Scale bar: $50\text{ }\mu\text{m}$. **e-f**, The SHG spatial mapping at 5 K after the first cooling (**e**) and the second cooling (**f**) on the thick sample. Light and dark green arrows show the direction nodes in the crossed polar pattern, which is close to the Néel vector direction. Scale bar: $50\text{ }\mu\text{m}$. Inset: crossed patterns on two sides of a domain wall with positions marked by orange and blue dots.

of high and nearly equal SHG intensity on both sides. In one of the regions, we pick up a few points such as the blue dot in Fig. 2e and observe the same polar patterns shown as blue in the top right of Fig. 2e. Crossing the dark line to a different region, we pick up a few points such as the orange one and observe the crossed polar patterns rotated by a small angle shown as orange on the top right of Fig. 2e. By keeping the laser spot at the orange point and performing a few thermal cycles, the polar pattern switches only between the blue and orange ones shown in Fig. 2e. We interpret the two regions with high SHG intensity as two different AFM domains where the spins are reversed by 180° under the time-reversal operation and the dark lines are domain walls due to destructive interference [34, 49]. The arrows in Fig. 2e,f indicate the opposite directions of the Néel vectors in different regions determined by SHG polar pattern measurements at 5 K. (See Supplementary Note 1.) A second SHG map after a thermal cycling across T_N in Fig. 2f shows that the domain wall is not pinned and different regions still only have the two kinds of polar patterns shown in 2e. (See the mapping on a $30\text{ }\mu\text{m}$ -thick naturally grown sample in Supplementary Figure 6.) The reason why we could observe the domain wall between two AFM regions with a π phase shift by the destructive SHG

interference is that the SHG has both ED and EQ contributions and only the ED term is sensitive to the π phase shift. One could write the signal we observe as $I_i(2\omega) \sim |\sum_{jk} \pm \chi_{ijk}^{ED}(\mathbf{L}) E_j(\omega) E_k(\omega) + \sum_{jkl} \chi_{ijkl}^{EQ} E_j(\omega) \nabla_k E_l(\omega)|^2$, where the \pm signs indicate the sign change of the ED term under time-reversal operation. As shown in Fig. 1b and 2a, the ED contribution at 5 K is ~ 200 times larger than the EQ part and therefore the two AFM domains have high and nearly equal SHG while the domain wall has very low SHG with the EQ contribution only.

Before we discuss the origin of the two-state Ising order instead of the six-state clock order, we investigate whether the AFM order exists and direct imaging of Néel vector switching could be detected in the monolayer first. The ultra-thin flakes down to the monolayer are exfoliated on SiO₂/Si wafers. The number of layers are determined by a combination of atomic force microscopy and optical contrast measurements [50]. (See Extended Data Figure 1.) To probe the intrinsic properties of the materials, we exfoliate samples down to the monolayer in a glove box. Fig. 3a shows the layer-dependent square root of the SHG intensity measured as a function of the temperature. All of the thin flakes show a clear phase transition down to the monolayer with the layer-dependent transition temperature shown in Fig. 3b. The transi-

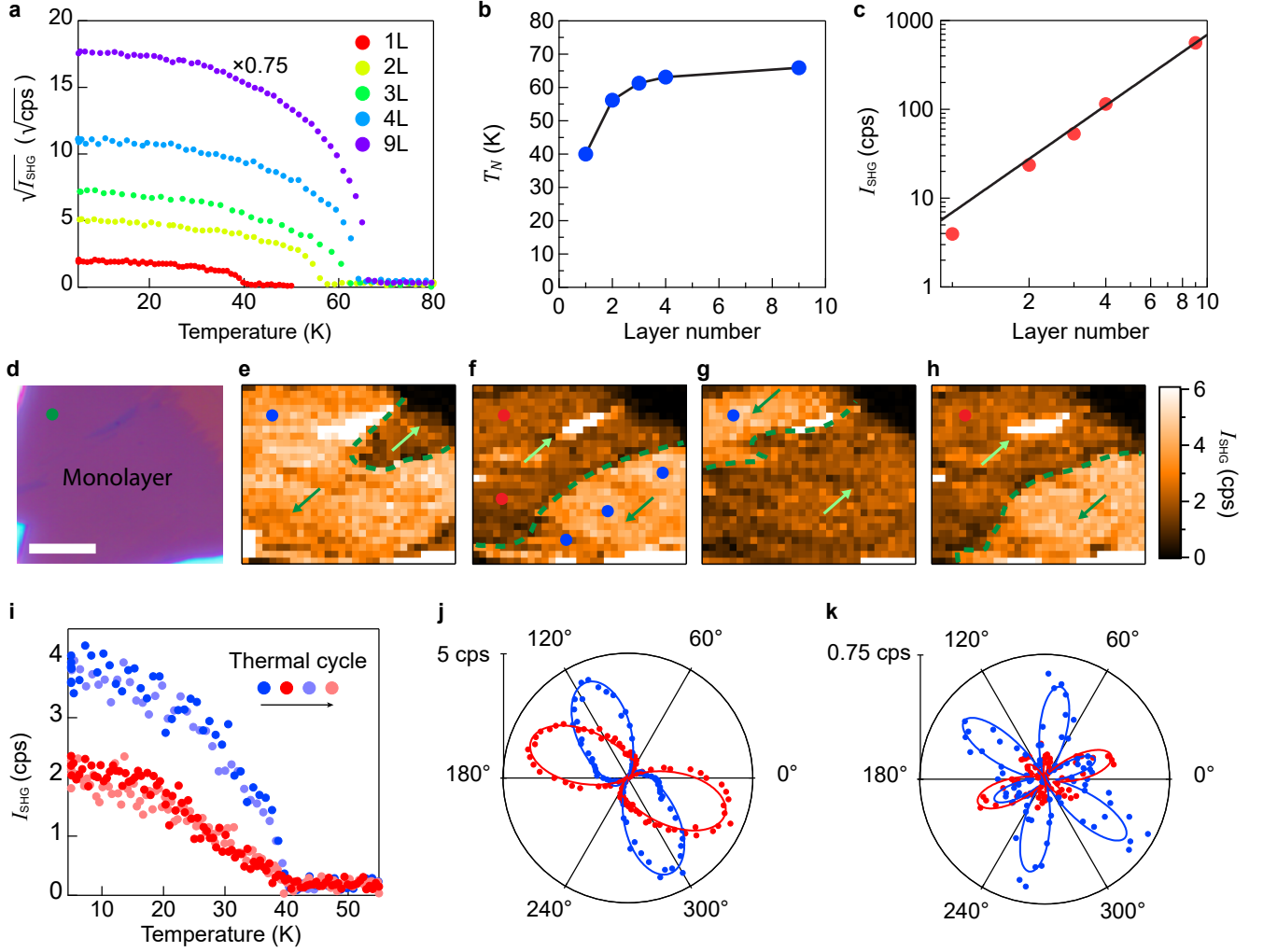


FIG. 3: **SHG and Néel vector switching of atomically-thin MnPSe_3 samples exfoliated in a glove box.** **a**, Temperature-dependent SHG response on samples with different layers. **b**, Layer-dependent Néel temperature. **c**, Layer-dependent SHG intensity in a log-log plot. The solid line is a fit for $I \sim N^2$. **d**, Optical image of a monolayer sample (S1). Scale bar: 10 μm . **e-h**, SHG intensity mapping over the monolayer sample at 5 K after different thermal cycles. The dark and the light regions represent two different domains where the Néel vector switches by 180° . The domain walls are highlighted by the green dashed lines. The Néel vectors in two domains are denoted by the green arrows. **i**, Temperature-dependent SHG intensity measured at the point marked by green in **(d)**. Curves from four different thermal cycles are shown. **j-k**, SHG polar patterns (**j**: crossed and **k**: parallel) for the two domains marked by red and blue, respectively. SHG polar patterns at the selected red and the blue dots in **(e-h)** are confirmed to have the same crossed pattern with the same color in **(j)**. See raw data in Extended Data Figure 4.

tion temperature decreases from 66 K in the nine-layer sample to 56 K in the bilayer sample and it is 40 K measured in three different monolayer samples (see Extended Data Figure 2-3 for the other two monolayer samples). The intensity of SHG at 5 K from 1 layer to 9 layers nearly follows a quadratic dependence on the layer count (Fig. 3c), which is expected for breaking the inversion symmetry in all these samples [51, 52]. This is different from synthetic layered AFM CrI_3 which supports SHG signals only with even numbers of layers [36]. Fig. 3d shows an optical image of the monolayer MnPSe_3 sample

1 (S1). We performed twelve thermal cycles at the green dot shown in Fig. 3d with the temperature-dependent SHG collapsed on two curves, and we plot four of them as examples in Fig. 3i. The corresponding polar patterns for the two AFM states are shown in Fig. 3j,k. Note that the change of the orientation in the crossed patterns in the monolayer is larger than that in bulk samples because of the reduced intensity ratio between the ED and EQ terms with reduced thickness. Fig. 3e-h shows four SHG maps at 5 K after thermal cycles and the green dashed lines are mobile AFM domain walls. All of them

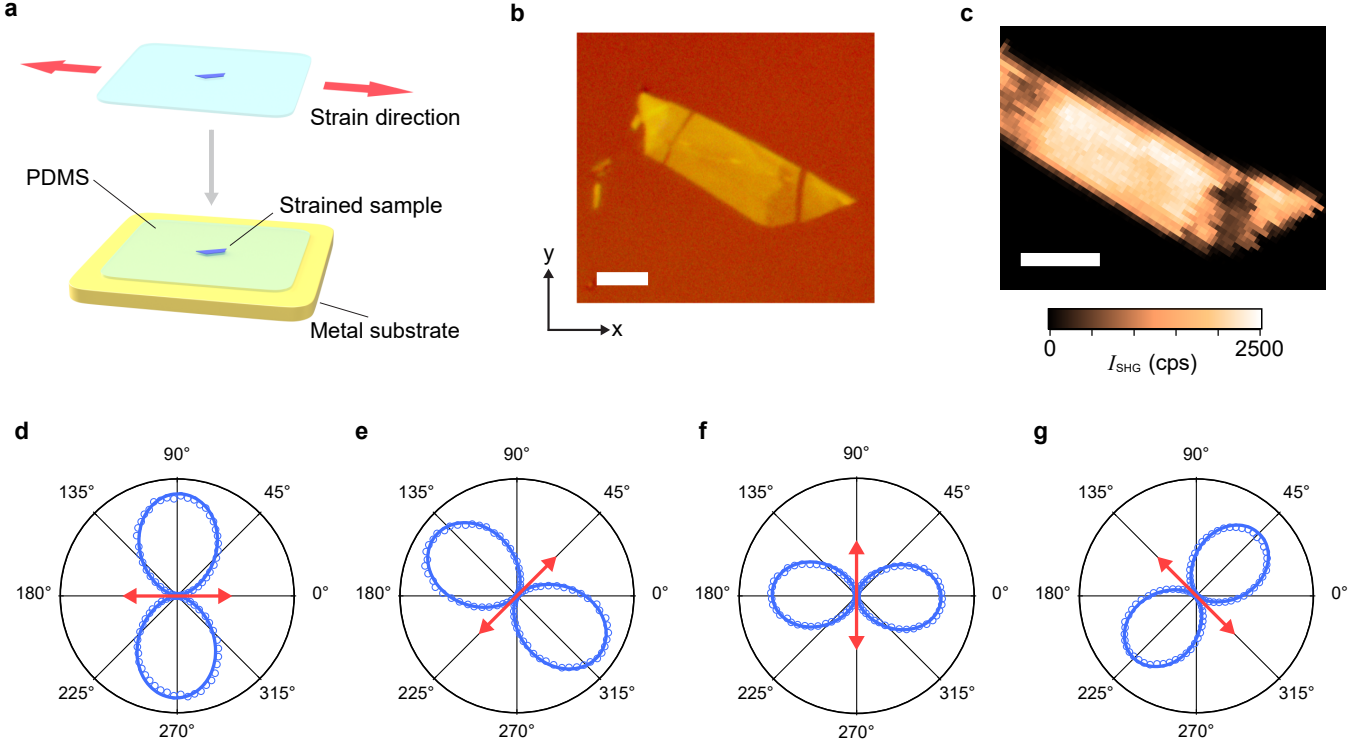


FIG. 4: **Strain-tunable Néel vector in MnPSe_3 .** **a**, A schematic of the method to control the in-plane strain. A MnPSe_3 flake is first exfoliated on a PDMS substrate. A tunable stretching force is then applied by a micro-manipulator on the PDMS to transfer strain to the sample, which is maintained by attaching the PDMS to a gold-coated sample holder. **b**, An optical image of a stretched 15 nm-thick MnPSe_3 flake with a uniaxial $\sim 2\%$ along the x axis. Scale bar: $10\ \mu\text{m}$. **c**, SHG spatial mapping with a 2% strain applied along x axis at nominally $5\ \text{K}$. Scale bar: $10\ \mu\text{m}$. **d-g**, Crossed polar patterns with strain direction along (d) 0° , (e) 45° , (f) 90° and (g) 135° with respect to the x axis. The red arrow represents the strain direction. The measured data are shown in blue open circles with fits shown in blue lines.

exhibit a contrast with two domains, with Fig. 3e showing a dominant bright domain. Measured polar patterns on selected dots marked by red and blue in Fig. 3e-h have the same red and blue patterns shown in Fig. 3j,k. (See Extended Data Figure 4 for more data.) We would like to point out that we observed a drop of T_N by 2-4 K in the bilayer and by 18 K in the monolayer due to aging effects when samples are exfoliated in air. (See Extended Data Figure 5.)

We observed the same two-state Ising order on all of the samples with thickness from monolayer to $\sim 30\ \mu\text{m}$ either exfoliated on SiO_2/Si or directly glued on the metal platform of the cryostat. All of them show two-fold crossed polar patterns, regardless whether they are prepared in air or in a glovebox. (See Extended Data Figure 2-6, Supplementary Figure 2, 4, 7 and 9.) Since the flakes are exfoliated on SiO_2 and the bulk μm -thick crystals are glued on the metal platform directly, a certain strain amount is inevitable. Therefore, we hypothesized that the Ising anisotropy is induced by the strain. In order to verify it, we deliberately apply a $\sim 2\%$ uniaxial strain by exfoliating a 15 nm flake on the polymer polydimethylsiloxane (PDMS) [6, 54] and then stretch the PDMS as shown in Fig. 4a. The strain strength is de-

termined by measuring the length of the optical image of the sample along the elongation direction shown in Fig. 4b before and after stretching (see Supplementary Figure 12 and Supplementary Note 4). The SHG mapping with $\sim 2\%$ strain along the x direction, shown in Fig. 4c, is quite homogeneous and the crossed polar patterns at different positions all point along the same direction (Fig. 4d.), which indicates that the strain aligns the Néel vector. We further apply the strain along 0° , 45° , 90° and 135° degrees with respect to the x axis defined in Fig. 4b and found that the crossed polar pattern follows the rotation of the strain as shown in Fig. 4d-g within the experimental accuracy of $\pm 10^\circ$, which indicates that the Néel vector is locked to the strain. We also demonstrated the Néel vector rotation by strain in a 3L sample. (See Extended Data Figure 7.) Because PDMS is transparent and reduces color contrast, the 3L sample is almost invisible on PDMS. (See Extended Data Figure 7.) Instead of direct straining of a monolayer on PDMS, we exfoliate a monolayer sample S3 with a long wavy shape on SiO_2/Si substrate to induce strain inhomogeneity in different regions, and find that Néel vector direction is also locked to the local strain and points to different directions in different regions. (See Extended Data Figure 3.)

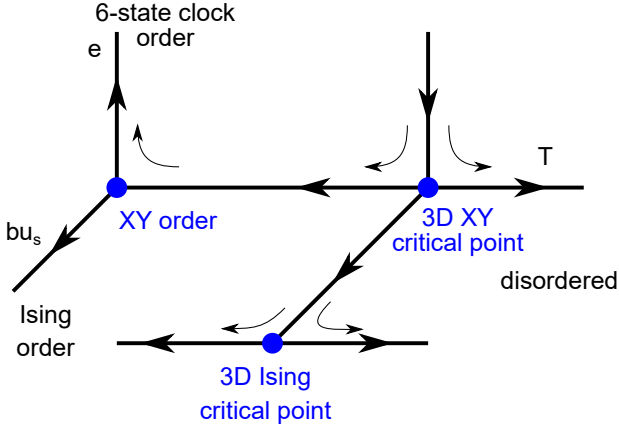


FIG. 5: **RG (Renormalization group) flow of the Landau theory.** When $\mu_s = 0$, it flows into the 3D XY critical point and develops the six-state clock order at low temperature. When $\mu_s \neq 0$, it flows into the 3D Ising critical point and develops the two-state Ising order at low temperature.

We also find that the parallel polar patterns are different between monolayers S1 and S2. Fittings of the patterns indicate that the relative angles between the Néel vector and the crystal axis are different among samples S1 and S2, indicating that strain directions in two samples are different. (See Extended Data Figure 2.) We would like to point out that the Néel vector could be rotated to any direction by the strain in atomically thin MnPSe_3 due to the strain-locked Ising order, which is drastically different from a non-XY system where Néel vectors are switched between principal crystal axes only [55]. We also noticed that the strain does not change the transition temperature, most likely because the strain-induced anisotropy is much smaller than the large XY anisotropy in this system [43]. (See Extended Data Figure 8, Supplementary Figure 13 and Supplementary Note 4.)

In order to understand why strain leads to an Ising order instead of a six-state clock order, we first employ a Landau expansion for free energy as a function of the Néel vector L , which applies close to the critical temperature when L is small. The lowest order term that accounts for the three-fold crystalline anisotropy, along with \mathcal{PT} symmetry, is $L^6 \cos 6\theta$, where θ is the polar angle measured from the a axis in Fig. 1a. The strain is described by a second-rank tensor whose principal axes designate the directions of tensile and compressive strain. It can be diagonalized with a rotation about the c axis by an angle θ_0 , and it provides the term $u_s L^2 \cos 2(\theta - \theta_0)$. Therefore, the θ dependent terms in the Landau free energy then take the form

$$F(\theta) = bu_s L_0^2 \cos 2(\theta - \theta_0) + eL_0^6 \cos 6\theta \quad (1)$$

Where b and e are coefficients, u_s is the amplitude of the strain and L_0 is the magnitude of the Néel vector. As shown in Fig. 5, for $u_s = 0$, in the absence of strain, this describes a six-state clock model, whose critical behavior is expected to be in the XY universality class. For $u_s \neq 0$, the Ising anisotropy dominates, and the critical behavior is in the Ising universality class [11, 12]. In general, the direction of the Néel vector will be determined by the competition between the strain and the crystalline anisotropy (See Supplementary Note 5.) This model explains why an Ising order is also induced in the $\sim 15 \mu\text{m}$ thick bulk sample mounted by glue as the strain is quite small.

These conclusions also follow from a more microscopic model of spins on a honeycomb lattice with interactions that reflect the symmetries of the crystal. We consider an XY model with nearest-neighbor couplings that are modified by strain and have the form

$$H = J_{\parallel,ij} \mathbf{s}_{i,\parallel} \mathbf{s}_{j,\parallel} + J_{\perp,ij} \mathbf{s}_{i,\perp} \cdot \mathbf{s}_{j,\perp} + J_c (\mathbf{s}_{i,\parallel} \mathbf{s}_{j,\perp} + \mathbf{s}_{i,\perp} \mathbf{s}_{j,\parallel}) \quad (2)$$

distinguishing the coupling for spin polarizations “along” ($J_{\parallel,ij}$) and “perpendicular to” ($J_{\perp,ij}$) the ij -th Mn-Mn bond and J_c is a symmetry allowed cross coupling between orthogonal spin components $s_{\parallel,ij}$ and $s_{\perp,ij}$ in each bond. The total energy is proportional to $|L|^2 \cos(2(\theta - \theta_0 - \alpha/2))$, where $\alpha/2$ defines a misalignment angle of the spin orientation from the principal strain axis. As long as the response is linear, decreasing the amount of strain while keeping the same direction will not change the tipping angle. (See Supplementary Note 6 for more details.)

The direct imaging of Néel vector switching in the monolayer goes beyond previous works of domain imaging in bulk AFM samples [34, 56, 57] and opens the possibility of ultra-compact AFM spintronics. Our work also creates a new method to control the 2D antiferromagnetism besides electric gating [22–24] and magnetic fields [36]. Additionally, our imaging and strain-tuning methods are generically applicable to other van der Waals AFM materials including the intrinsic AFM topological insulator [58]. Looking forward, we hope that the discovery of extremely strain-tunable AFM order in atomically thin MnPSe_3 would stimulate further investigations in designing spatial strain patterns, to create spin pattern on demand for magnon propagation in low-dissipation terahertz spintronic devices. The monolayer MnPSe_3 also provides a platform to study the Kosterlitz-Thouless transition in a truly 2D XY magnet with six-state clock order if the strain could be tuned to zero by a voltage-controlled piezo-stage [59]. The atomically thin MnPSe_3 might also be a good candidate for broadband, efficient upper-conversion as the gap is in the visible regime.

[1] Costanzo, D., Jo, S., Berger, H. & Morpurgo, A. F. Gate-induced superconductivity in atomically thin MoS_2 crys-

als. *Nature Nanotechnology* **11**, 339–344 (2016).

- [2] Xi, X. *et al.* Strongly enhanced charge-density-wave order in monolayer NbSe₂. *Nature Nanotechnology* **10**, 765–769 (2015).
- [3] Wu, S. *et al.* Observation of the quantum spin Hall effect up to 100 kelvin in a monolayer crystal. *Science* **359**, 76–79 (2018).
- [4] Huang, B. *et al.* Layer-dependent ferromagnetism in a van der Waals crystal down to the monolayer limit. *Nature* **546**, 270–273 (2017).
- [5] Mak, K. F., Shan, J. & Ralph, D. C. Probing and controlling magnetic states in 2D layered magnetic materials. *Nature Reviews Physics* **1**, 646–661 (2019).
- [6] Némec, P., Fiebig, M., Kampfrath, T. & Kimel, A. V. Antiferromagnetic opto-spintronics. *Nature Physics* **14**, 229–241 (2018).
- [7] Wadley, P. *et al.* Electrical switching of an antiferromagnet. *Science* **351**, 587–590 (2016).
- [8] Saidl, V. *et al.* Optical determination of the Néel vector in a CuMnAs thin-film antiferromagnet. *Nature Photonics* **11**, 91–96 (2017).
- [9] Cheong, S.-W., Fiebig, M., Wu, W., Chapon, L. & Kiryukhin, V. Seeing is believing: visualization of antiferromagnetic domains. *npj Quantum Materials* **5**, 3 (2020).
- [10] Nair, N. L. *et al.* Electrical switching in a magnetically intercalated transition metal dichalcogenide. *Nature Materials* **19**, 153–157 (2020).
- [11] Oshikawa, M. Ordered phase and scaling in Zn models and the three-state antiferromagnetic Potts model in three dimensions. *Physical Review B* **61**, 3430 (2000).
- [12] Lou, J., Sandvik, A. W. & Balents, L. Emergence of U(1) Symmetry in the 3D XY Model with Z_q Anisotropy. *Physical Review Letters* **99**, 207203 (2007).
- [13] Cheong, S.-W. SOS: symmetry-operational similarity. *npj Quantum Materials* **4**, 53 (2019).
- [14] Gong, C. *et al.* Discovery of intrinsic ferromagnetism in two-dimensional van der Waals crystals. *Nature* **546**, 265–269 (2017).
- [15] Deng, Y. *et al.* Gate-tunable room-temperature ferromagnetism in two-dimensional Fe₃GeTe₂. *Nature* **563**, 94–99 (2018).
- [16] Fei, Z. *et al.* Two-dimensional itinerant ferromagnetism in atomically thin Fe₃GeTe₂. *Nature Materials* **17**, 778–782 (2018).
- [17] Thiel, L. *et al.* Probing magnetism in 2D materials at the nanoscale with single-spin microscopy. *Science* **364**, 973–976 (2019).
- [18] Chen, W. *et al.* Direct observation of van der Waals stacking dependent interlayer magnetism. *Science* **366**, 983–987 (2019).
- [19] Song, T. *et al.* Giant tunneling magnetoresistance in spin-filter van der Waals heterostructures. *Science* **360**, 1214–1218 (2018).
- [20] Klein, D. R. *et al.* Probing magnetism in 2D van der Waals crystalline insulators via electron tunneling. *Science* **360**, 1218–1222 (2018).
- [21] Wang, Z. *et al.* Very large tunneling magnetoresistance in layered magnetic semiconductor CrI₃. *Nature Communications* **9**, 2516 (2018).
- [22] Huang, B. *et al.* Electrical control of 2D magnetism in bilayer CrI₃. *Nature Nanotechnology* **13**, 544–548 (2018).
- [23] Jiang, S., Shan, J. & Mak, K. F. Electric-field switching of two-dimensional van der Waals magnets. *Nature Materials* **17**, 406–410 (2018).
- [24] Jiang, S., Li, L., Wang, Z., Mak, K. F. & Shan, J. Controlling magnetism in 2D CrI₃ by electrostatic doping. *Nature Nanotechnology* **13**, 549–553 (2018).
- [25] Burch, K. S., Mandrus, D. & Park, J.-G. Magnetism in two-dimensional van der Waals materials. *Nature* **563**, 47–52 (2018).
- [26] Gong, C. & Zhang, X. Two-dimensional magnetic crystals and emergent heterostructure devices. *Science* **363** (2019).
- [27] Gibertini, M., Koperski, M., Morpurgo, A. & Novoselov, K. Magnetic 2D materials and heterostructures. *Nature Nanotechnology* **14**, 408–419 (2019).
- [28] Lee, J.-U. *et al.* Ising-type magnetic ordering in atomically thin FePS₃. *Nano Letters* **16**, 7433–7438 (2016).
- [29] Wang, X. *et al.* Raman spectroscopy of atomically thin two-dimensional magnetic iron phosphorus trisulfide (FePS₃) crystals. *2D Materials* **3**, 031009 (2016).
- [30] Kim, K. *et al.* Antiferromagnetic ordering in van der Waals 2D magnetic material MnPS₃ probed by Raman spectroscopy. *2D Materials* **6**, 041001 (2019).
- [31] Václavkova, D. *et al.* Magnetoelastic interaction in the two-dimensional magnetic material MnPS₃ studied by first principles calculations and Raman experiments. *2D Materials* (2020).
- [32] Huang, B. *et al.* Emergent phenomena and proximity effects in two-dimensional magnets and heterostructures. *Nature Materials* 1–14 (2020).
- [33] Long, G. *et al.* Persistence of Magnetism in Atomically Thin MnPS₃ Crystals. *Nano Letters* **20**, 2452–2459 (2020). PMID: 32142288.
- [34] Fiebig, M., Pavlov, V. V. & Pisarev, R. V. Second-harmonic generation as a tool for studying electronic and magnetic structures of crystals. *JOSA B* **22**, 96–118 (2005).
- [35] Chu, H. *et al.* Linear magnetoelectric phase in ultrathin MnPS₃ probed by optical second harmonic generation. *Physical Review Letters* **124**, 027601 (2020).
- [36] Sun, Z. *et al.* Giant nonreciprocal second-harmonic generation from antiferromagnetic bilayer CrI₃. *Nature* **572**, 497–501 (2019).
- [37] Wiedenmann, A., Rossat-Mignod, J., Louisy, A., Brec, R. & Rouxel, J. Neutron diffraction study of the layered compounds MnPSe₃ and FePSe₃. *Solid State Communications* **40**, 1067–1072 (1981).
- [38] Wildes, A., Roessli, B., Lebech, B. & Godfrey, K. Spin waves and the critical behaviour of the magnetization in MnPS₃. *Journal of Physics: Condensed Matter* **10**, 6417 (1998).
- [39] Wildes, A., Rule, K. C., Bewley, R., Enderle, M. & Hicks, T. J. The magnon dynamics and spin exchange parameters of FePS₃. *Journal of Physics: Condensed Matter* **24**, 416004 (2012).
- [40] Wildes, A. R. *et al.* Magnetic structure of the quasi-two-dimensional antiferromagnet NiPS₃. *Physical Review B* **92**, 224408 (2015).
- [41] Ressouche, E. *et al.* Magnetoelectric MnPS₃ as a candidate for ferrotoroidicity. *Physical Review B* **82**, 100408 (2010).
- [42] Lançon, D. *et al.* Magnetic structure and magnon dynamics of the quasi-two-dimensional antiferromagnet FePS₃. *Physical Review B* **94**, 214407 (2016).
- [43] Jeevanandam, P. & Vasudevan, S. Magnetism in MnPSe₃: a layered 3d⁵ antiferromagnet with unusually large XY anisotropy. *Journal of Physics: Condensed Matter* **11**, 3563 (1999).

- [44] Kim, K. *et al.* Suppression of magnetic ordering in XXZ-type antiferromagnetic monolayer NiPS₃. *Nature Communications* **10**, 345 (2019).
- [45] Kang, S. *et al.* Coherent many-body exciton in van der Waals antiferromagnet NiPS₃. *Nature* **583**, 785–789 (2020).
- [46] Wu, L. *et al.* Giant anisotropic nonlinear optical response in transition metal monophenictide Weyl semimetals. *Nature Physics* **13**, 350–355 (2017).
- [47] Sa, D., Valenti, R. & Gros, C. A generalized Ginzburg-Landau approach to second harmonic generation. *The European Physical Journal B-Condensed Matter and Complex Systems* **14**, 301–305 (2000).
- [48] Li, X., Cao, T., Niu, Q., Shi, J. & Feng, J. Coupling the valley degree of freedom to antiferromagnetic order. *Proceedings of the National Academy of Sciences* **110**, 3738–3742 (2013).
- [49] Yin, X. *et al.* Edge nonlinear optics on a MoS₂ atomic monolayer. *Science* **344**, 488–490 (2014).
- [50] Casiraghi, C. *et al.* Rayleigh imaging of graphene and graphene layers. *Nano Letters* **7**, 2711–2717 (2007).
- [51] Zhao, M. *et al.* Atomically phase-matched second-harmonic generation in a 2D crystal. *Light: Science & Applications* **5**, e16131–e16131 (2016).
- [52] Liu, F. *et al.* Disassembling 2D van der Waals crystals into macroscopic monolayers and reassembling into artificial lattices. *Science* **367**, 903–906 (2020).
- [53] Liu, Z. *et al.* Strain and structure heterogeneity in MoS₂ atomic layers grown by chemical vapour deposition. *Nature Communications* **5**, 5246 (2014).
- [54] Zhang, Q. *et al.* Strain relaxation of monolayer WS₂ on plastic substrate. *Advanced Functional Materials* **26**, 8707–8714 (2016).
- [55] Chen, X. *et al.* Electric field control of néel spin-orbit torque in an antiferromagnet. *Nature Materials* **18**, 931–935 (2019).
- [56] Fiebig, M. Revival of the magnetoelectric effect. *Journal of Physics D: Applied Physics* **38**, R123 (2005).
- [57] Wadley, P. *et al.* Current polarity-dependent manipulation of antiferromagnetic domains. *Nature Nanotechnology* **13**, 362–365 (2018).
- [58] Otrokov, M. M. *et al.* Prediction and observation of an antiferromagnetic topological insulator. *Nature* **576**, 416–422 (2019).
- [59] Mutch, J. *et al.* Evidence for a strain-tuned topological phase transition in ZrTe₅. *Science Advances* **5**, eaav9771 (2019).

I. Methods

Sample Preparation

Single crystals of MnPSe₃ were grown by the chemical vapor transport method. Elemental powders of high purity Mn, P, and Se were pressed into a pellet and sealed inside a quartz tube under vacuum. The tube was then annealed for a week at 730 °C to form polycrystalline MnPSe₃ powder, the composition of which was verified with powder X-ray diffraction. Crystals were then grown using the chemical vapor transport method with iodine as transport agent: 2 g of the powder and 0.4 g of io-

dine crystals were placed at the end of a quartz tube, which was sealed off at 13 cm length under vacuum. The sealed tube was then set in a temperature gradient of 650/525 °C for four days to transport the starting materials placed at the hot end to the cold end. The Mn : P : Se ratio was measured to be 1.00(1) : 0.96(1) : 3.07(1) with energy-dispersive X-ray spectroscopy. The ultra-thin samples were prepared by a standard mechanical exfoliation process on Si substrates with 90 nm thick SiO₂ from a few MnPSe₃ bulk crystals with $T_N \sim 68$ K. The samples were put into a vacuum environment after exfoliation. The total exposure time in air for samples exfoliated in a glove box is less than one minute before loading into the cryostat where the sample is under vacuum.

SHG microscopy

The sample was loaded on a metal platform in a closed-cycle cryostat, and the temperature of the metal platform was controlled by a local heater, which induces only a sub-micron shift of the sample position between 5 K and 100 K. An ultrafast 800-nm Ti-sapphire laser pulse with a duration ~ 50 fs at the repetition rate of 80 MHz was focused onto a 2 μ m beam spot on the sample under normal incidence. A typical laser power of 200 μ W was used except for the following cases. 500 μ W was used for thick flakes and bulk crystals. In the bilayer sample in Extended Data Figure 6, 400 μ W was used. No sample damage was observed during the measurement. The reflected SHG light was collected by an 50 \times objective and reflected by a dichroic mirror or a D mirror into a photomultiplier tube connected with a lock-in amplifier or a photon counter. The photon counter was locked to the 80 MHz in order to reduce the dark count below 0.2 counts per second (cps) without cooling the photomultiplier by cryogen. The detection sensitivity in the experiments was 0.2 counts per second. Because the parallel signal is one order smaller than the crossed signal, the polarization extinction ratio was important when measuring parallel patterns. The polarization of the fundamental light was controlled by a half-wave plate as well as a linear polarizer. The polarization of second-harmonic light was analyzed by a linear polarizer. The SHG imaging microscopy was achieved by moving the sample with three Attocube nano-positioners.

Strain Tuning

We exfoliated MnPSe₃ on PDMS with a square shape and applied tensile strain on two sides of the PDMS by a micro-manipulator. The stretched PDMS was then attached to a gold-coated sample platform. The strain was estimated by measuring the length change along the stretching direction in the optical image. A low transfer ratio ($\sim 13\%$) from PDMS to the sample was observed.

To change the sample's strain direction, we peeled off the PDMS from the sample platform and then stretched it in another direction. To apply strain along the 45° and 135° , we cut the four corners of the PDMS to form a smaller square shape in order to reduce twisting while applying strain. The error bar of estimation of strain strength is $\pm 0.5\%$ and the error bar of the strain direction is $\pm 10^\circ$.

Symmetry analysis for SHG polar patterns

For the SHG patterns above T_N , the angle dependence are described by

$$I_{\text{parallel}}(2\omega, \phi) \propto |\chi_{xxx}^{EQ} \cos 3\phi + \chi_{yxx}^{EQ} \sin 3\phi|^2, \quad (3)$$

$$I_{\text{crossed}}(2\omega, \phi) \propto |\chi_{xxx}^{EQ} \sin 3\phi - \chi_{yxx}^{EQ} \cos 3\phi|^2. \quad (4)$$

ϕ is the angle of the incident linear polarization with respect to the a axis of the crystal. Note that in the fit there is also a constant angle shift in ϕ , which is the angle between the horizontal axis in the lab and the crystal a axis. For the SHG patterns below T_N , we fit the crossed polar pattern by

$$I_{\text{crossed}}(2\omega, \phi, \theta) \propto L^2 |\sin(\phi - \theta)|^2, \quad (5)$$

and denote the node direction in the polar pattern as the Néel vector direction. θ is the angle of the direction of the Néel vector with respect to the crystal a axis. See Supplementary Note 1 for more details.

II. Acknowledgement

We thank S.W. Cheong and O. Tchernyshyov for helpful discussions. This project is mainly supported by L.W.'s startup package at the University of Pennsylvania. The development of the SHG photon counter was supported by the ARO YIP award under the Grant W911NF1910342 (L.W.). The measurement by the atomic force microscopy was supported by the ARO MURI award under the Grant W911NF2020166 (L.W.). The acquisition of the oscillator laser for the SHG experiment was supported by NSF through Penn MRSEC (DMR-1720530). E.J.M. acknowledges support from NSF EAGER 1838456. C.L.K. was supported by a Simons Investigator grant from the Simons Foundation. D.G.M. acknowledges support from the Gordon and Betty Moore Foundation's EPiQS Initiative, Grant GBMF9069. H.W. and X.Q. acknowledge support from NSF DMR-1753054 and Texas A&M University President's Excellence Fund X-Grants Program. B.X. and C.B. are supported by the Schweizerische Nationalfonds (SNF) by Grant No. 200020-172611. The DFT calculations were conducted with the advanced computing resources provided by Texas A&M High Performance Research Computing.

III. Author Contribution

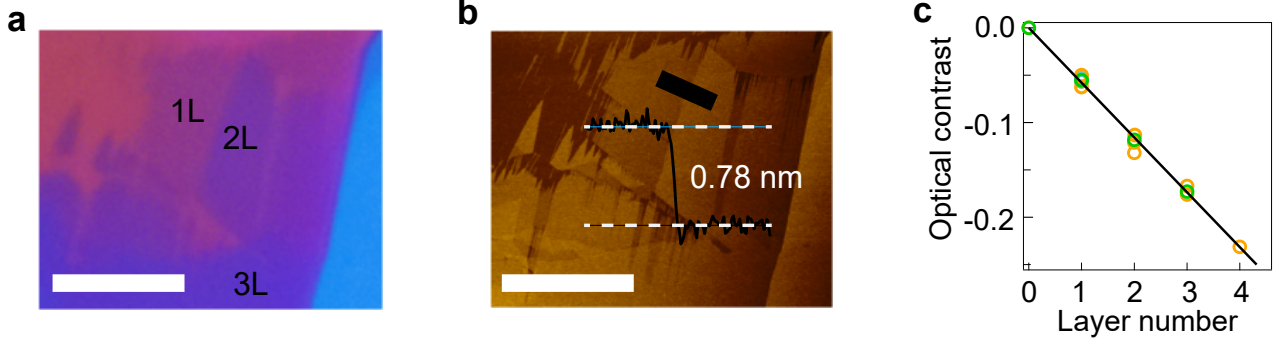
L.W. conceived the project and coordinated the experiments and theory. L.W. designed the SHG imaging setup and built it with Z.N.. Z.N. performed the experiments and analyzed the data under the supervision of L.W.. L.W., Z.N., E.M., and C.K. discussed and interpreted the data. E.M. performed the spin model calculation. C.K. performed the Landau theory calculation. A.H. and D.M. grew the crystals and performed magnetization measurements. H.W. and X.Q. performed first-principle calculation. B.X. and C.B. performed the optical conductivity measurement. L.W. and Z.N. wrote the manuscript from input of all authors. All authors edited the manuscript.

IV. Addendum

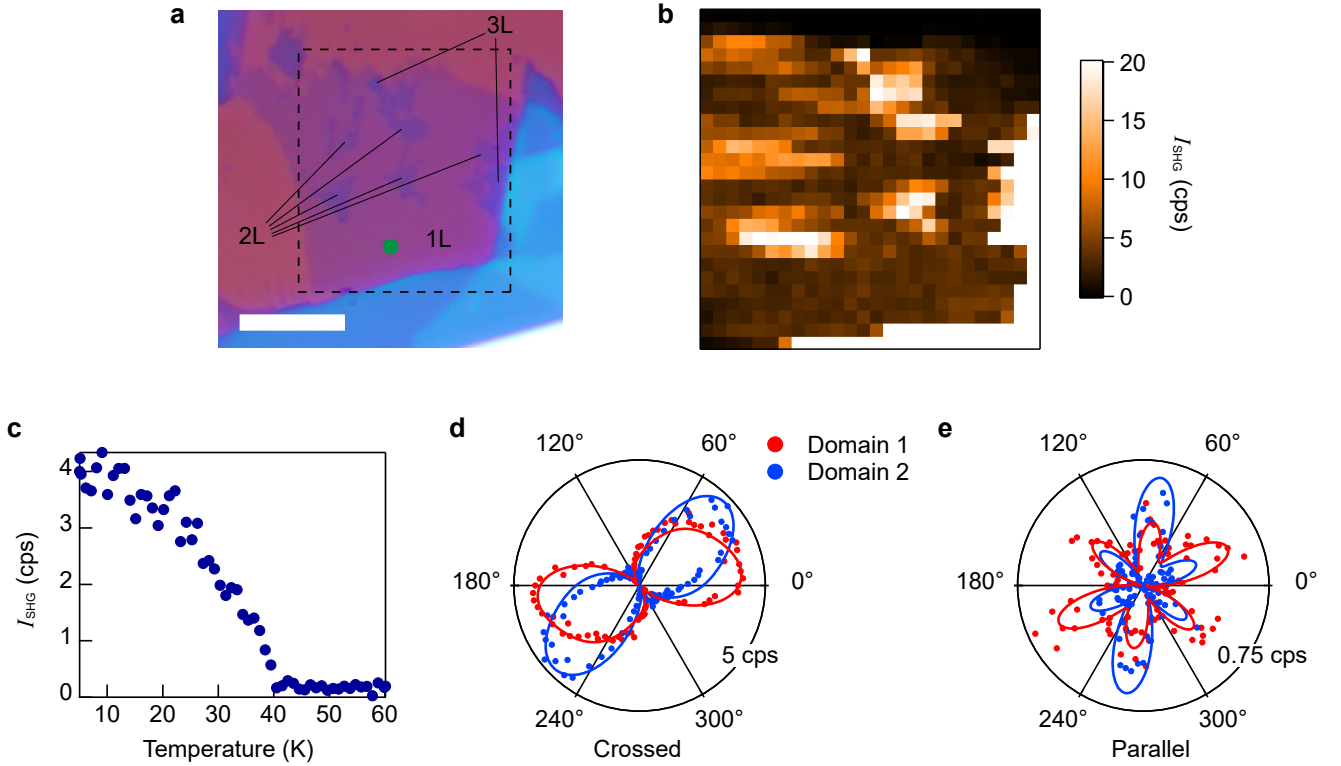
Data availability: All data needed to evaluate the conclusions in the paper are present in the paper and the Supplementary Information. Additional data related to this paper could be requested from the authors.

Competing Interests: The authors declare that they have no competing financial interests.

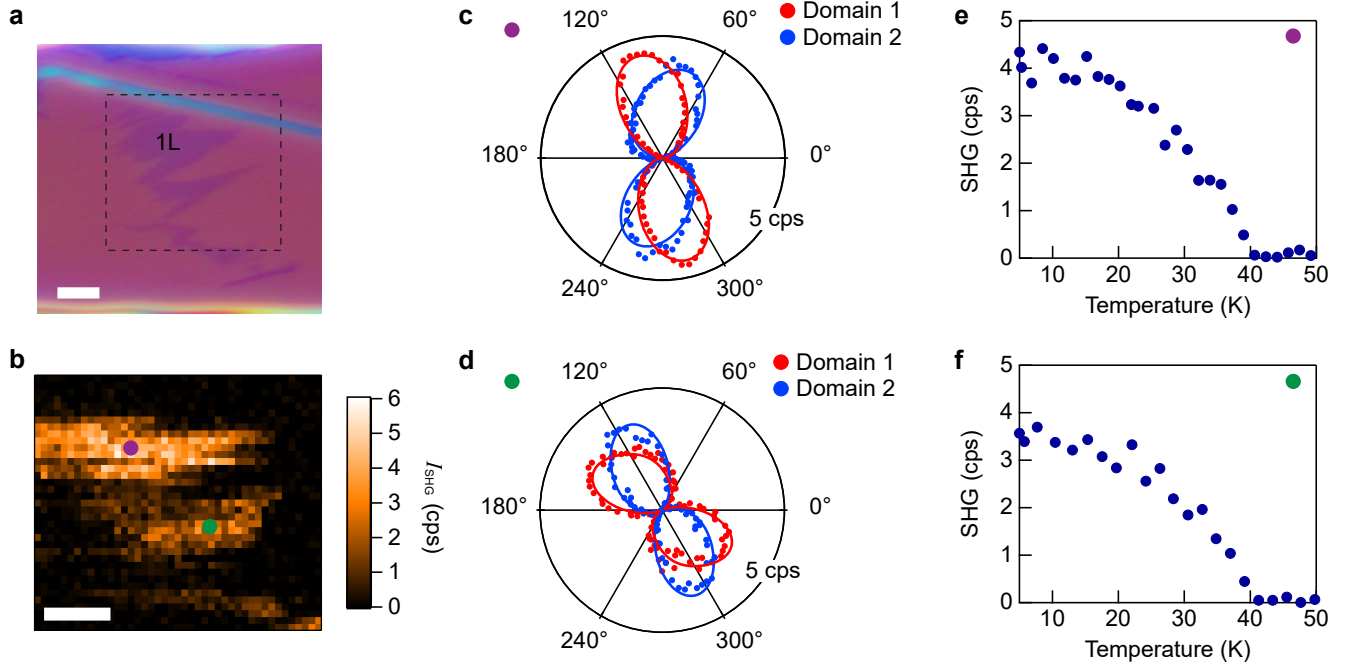
Correspondence: Correspondence and requests for materials should be addressed to L.W. (liangwu@sas.upenn.edu)



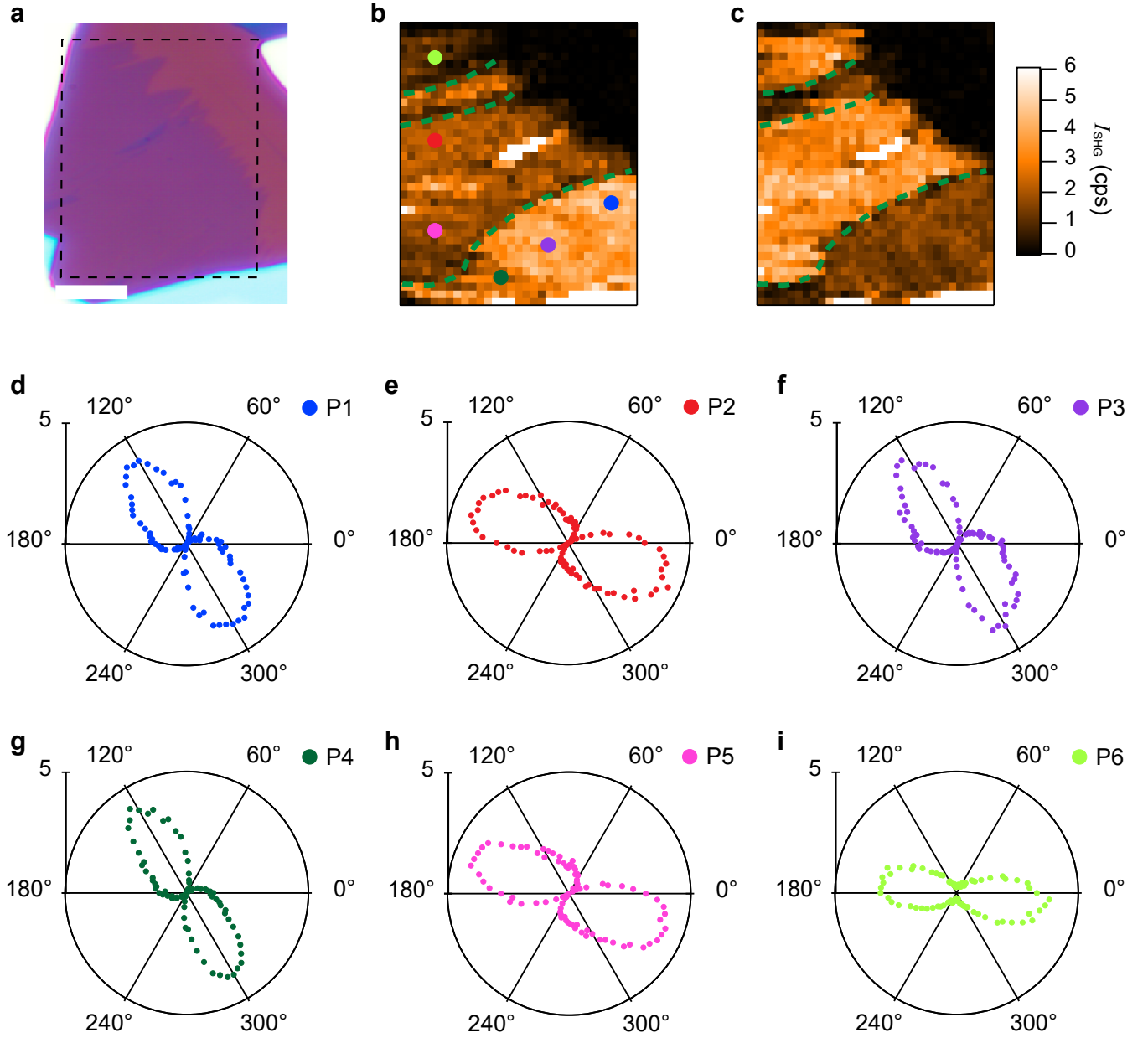
Extended Data Figure 1: Thickness characterization of atomically thin MnPSe₃ samples. **a**, Optical image of a multilayer MnPSe₃ exfoliated on the 90 nm SiO₂/Si substrate. Scale bar: 10 μ m. **b**, Atomic force microscopy image of the same sample in (a). The step between monolayer and bilayer is measured to be around 0.78 nm. Scale bar: 10 μ m. **c**, Optical contrast of samples with different layer numbers. Green circles are data extracted from sample shown in (a) and orange circles are data from other samples. The black line is a linear fit.



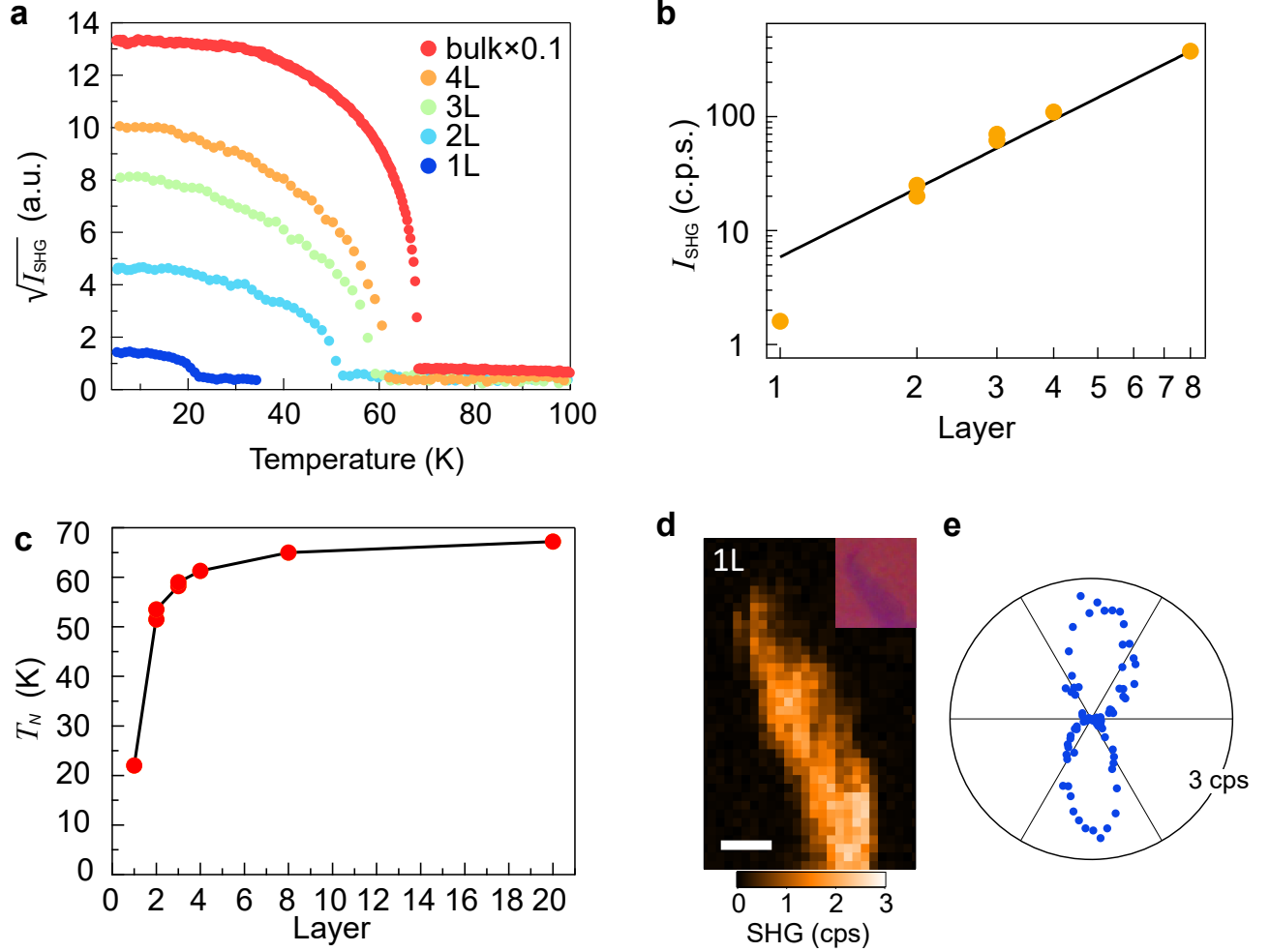
Extended Data Figure 2: SHG data for monolayer S2 exfoliated in a glove box. **a**, Optical image of the monolayer S2. There are some small bilayer/trilayer islands inside the monolayer sample. Scale bar: 10 μ m. The dashed region is the area for SHG mapping. **b**, SHG intensity mapping of the monolayer S2. **c**, SHG intensity as a function of temperature measured at the green point marked in (a) for one thermal cycle. **d-e**, Polarization-dependent SHG patterns measured at the green point in the crossed (d) and the parallel (e) configuration after two different thermal cycles. Data from both domains are shown. The dots are experimental data and the solid lines are the best fit. The patterns are different from the monolayer S1, indicating the angles between the Néel vector and the crystalline axis are different in the two samples.



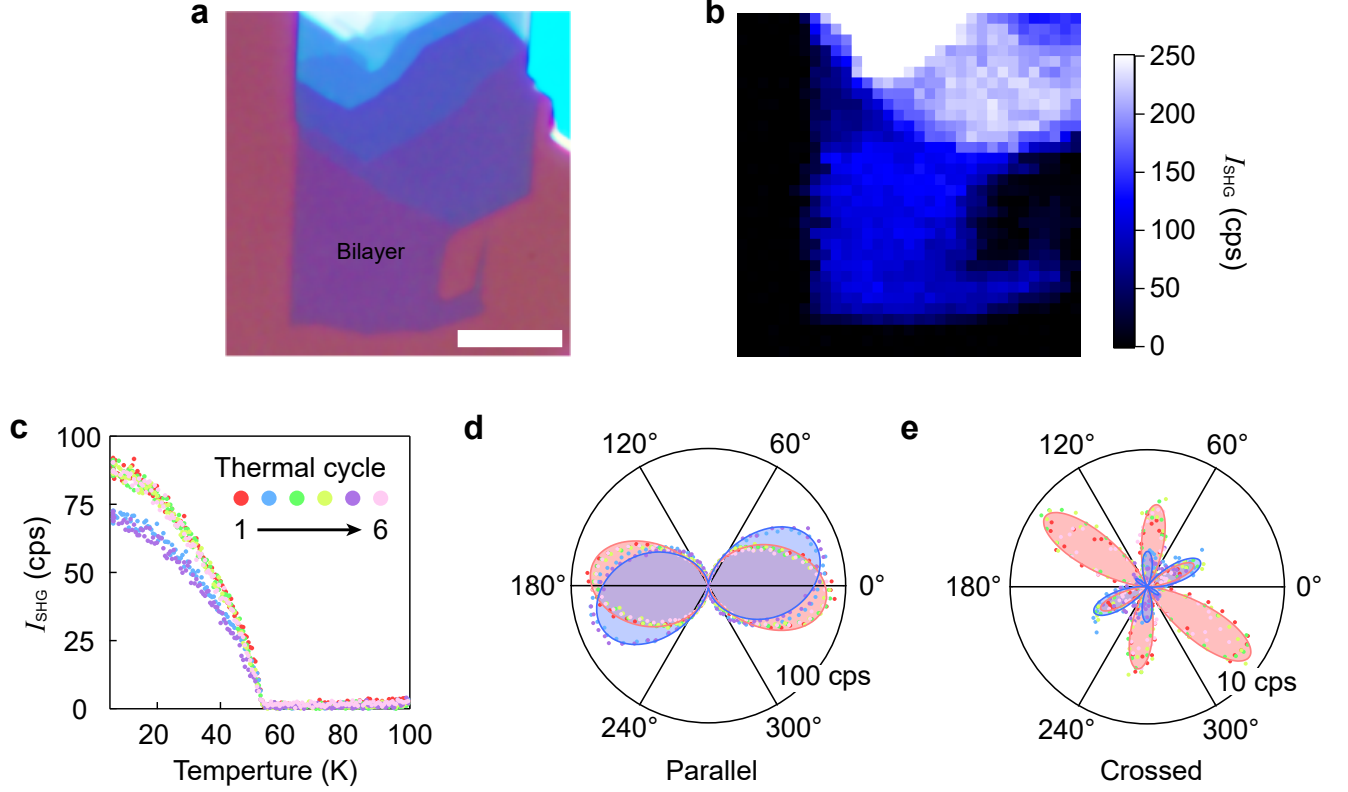
Extended Data Figure 3: SHG data for monolayer S3 exfoliated in a glove box. **a**, Optical image of the monolayer S3. Scale bar: 10 μm . The dashed box denotes the region of SHG mapping. **b**, SHG intensity mapping of the monolayer S3. Scale bar: 10 μm . Polar patterns at the two points denoted by purple and green dots are measured after thermal cycles. **c**, Crossed patterns of two domains of the purple point measured at 5 K after two different thermal cycles. **d**, Crossed patterns of two domains of the green point measured at 5 K after two different thermal cycles. **e**, SHG intensity as a function of temperature at the purple point for one thermal cycle. **f**, SHG intensity as a function of temperature at the green point for one thermal cycle. Different crossed polar patterns also with different orientations at the purple and the green points indicate that their Néel vectors have different directions.



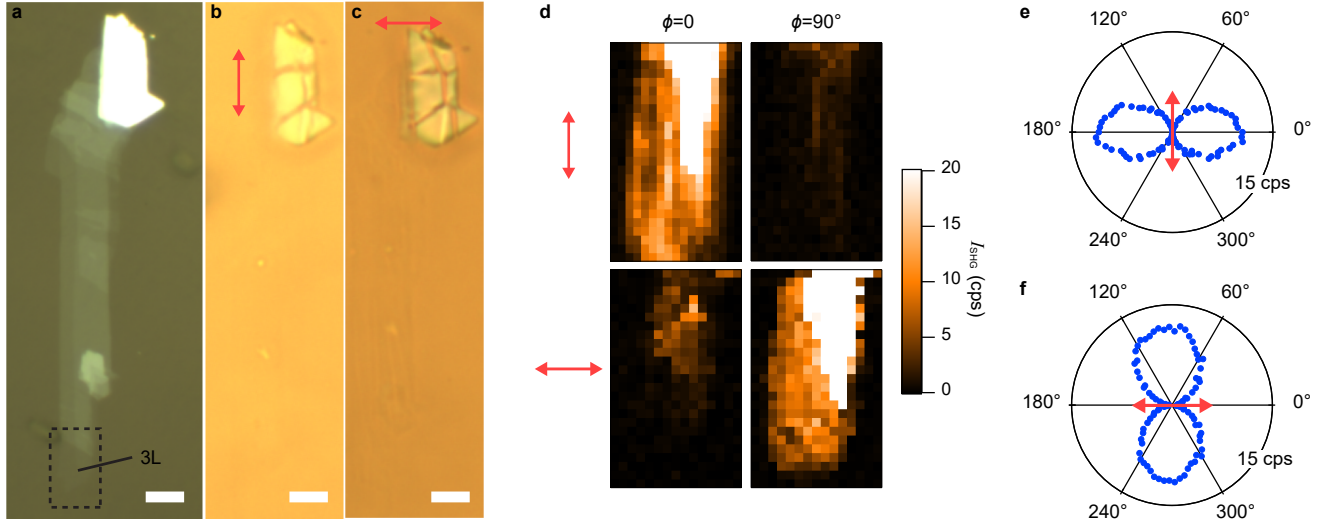
Extended Data Figure 4: More data of the monolayer S1 shown in the main text. a, Optical image of the sample S1. Scale bar: $10\ \mu\text{m}$. The dashed region is the area for SHG mapping. **b**, SHG intensity mapping at $\phi = 120^\circ$ (the peak of domain 1) in the crossed pattern. **c**, SHG intensity mapping at $\phi = 160^\circ$ (the peak of domain 2) in the crossed pattern. Maps in (b,c) are after the same thermal cycle. The domain walls are highlighted by the green dashed lines. **d-i**, Crossed patterns of six different points marked by different colors in (b). The measurement is performed at 5 K. P1-P5 are the same points in Fig. 3f in the main text. P6 is very close to sample corner and displays smaller SHG intensity with a slightly different orientation, which indicates the Néel vector at P6 has a slightly different direction.



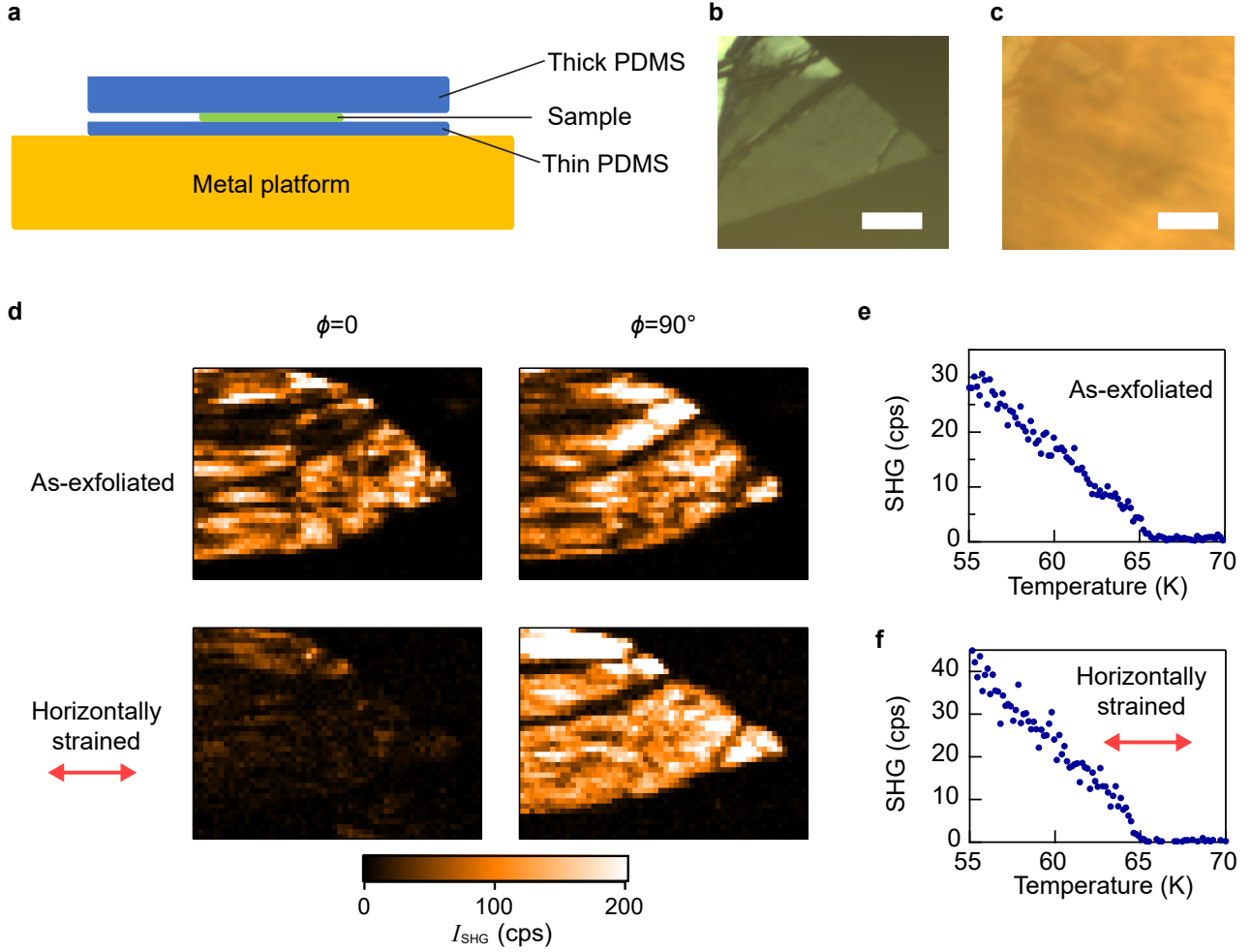
Extended Data Figure 5: SHG data of atomically thin samples exfoliated in air. **a**, Square root of the SHG intensity as a function of temperature in samples with different thickness. All of the samples in this figure are exfoliated in air. **b**, SHG intensity at 5 K as a function of layer numbers in a log-log plot. Data are shown in yellow dots. The solid line is a fit for $I \propto N^2$. **c**, Néel temperature as a function of layer numbers. Note that there is a large reduction of both SHG signal and Néel temperature of monolayer compared to those exfoliated in the glove box due to the aging effect. See more data on the aging effect on a bilayer sample in Supplementary Figure 10. **d**, SHG intensity mapping of a monolayer MnPSe₃ exfoliated in air at 5 K. Scale bar: 3 μm . Inset: Optical image of the monolayer sample. **e**, Crossed polar pattern measured at the center of the monolayer sample shown in **d** at 5 K.



Extended Data Figure 6: SHG data for a bilayer sample exfoliated in air. This sample is exfoliated in air and different from the sample shown in the main text, which is exfoliated in a glove box. **a**, Optical image of the bilayer sample. Scale bar: 10 μm . **b**, SHG intensity mapping of the bilayer sample at 5 K. Note that the SHG intensity of this sample is quite uniform, which indicates that the Néel vector direction is nearly aligned. **c**, SHG intensity of 6 consecutive cooling runs across T_N . The curves collapse into two, indicating the existence of two domains. **d-e**, Crossed (**d**) and parallel (**e**) polar patterns measured after each cooling at 5 K. The measured data are shown in dots. The blue and red shaded regions are guides for the eye, corresponding to the two different AFM domains.



Extended Data Figure 7: Strain tunability of Néel vector of a trilayer sample. The strained sample is prepared using the same method as in the main text. The measured thickness is around 3.2 nm, which is a typical thickness for a trilayer sample. The measured Néel temperature is also consistent with a typical trilayer sample. **a**, Optical image of the sample exfoliated on the PDMS before adding strains. The trilayer sample is marked by the black box. Scale bar: 10 μm . **b-c**, Optical image of the sample when vertical and horizontal strains are added (marked by the red arrows), respectively. The sample and PDMS are mounted on the metal platform and the contrast of the sample is low. A 5% strain is added on the PDMS by a micro-manipulator. The direction of the cracks of the thick flake on the top also indicates the strain direction. **d**, SHG intensity mapping of the dashed area in (a) under different strain direction (marked by the red arrows) and ϕ in the crossed pattern. The dark intensity maps in (d) indicate that the Néel vectors are mainly along the strain direction, and rotated by around 90° when the strain direction is switched from vertical to horizontal. **e**, Crossed pattern at the center of the trilayer sample with vertical strain direction. **f**, Crossed pattern at the center of the trilayer sample with horizontal strain direction. All of the above SHG measurements are operated at 5 K.



Extended Data Figure 8: Strain dependence on the Néel temperature of a MnPSe_3 sample. The MnPSe_3 samples in the strain-tuning experiment are exfoliated on a $\sim 30 \mu\text{m}$ PDMS, which is too thick to have the best thermal conductance. One needs to calibrate the sample temperature by measuring a thick flake on the same PDMS each time. To measure the sample temperature without calibration, we use thinner home-made ($\sim 5 \mu\text{m}$) PDMS to increase the thermal conductance and encapsulate the sample after exfoliation and attach the thinner PDMS to the metal platform after applying strain (shown in **a**). **b**, Optical image of an as-exfoliated sample ($\sim 8 \text{ L}$) on the PDMS substrate before being put onto the metal platform. Scale bar: $10 \mu\text{m}$. **c**, Optical image of the same sample under a horizontal strain. A 5% strain on PDMS is added by a micromanipulator and then the PDMS is attached to the metal platform. Scale bar: $10 \mu\text{m}$. **d**, SHG intensity mappings of the as-exfoliated and strained sample measured at $\phi = 0^\circ$ and $\phi = 90^\circ$ in the crossed polar pattern. The as-exfoliated sample shows that the Néel vectors are not oriented horizontally while the strained sample favors a horizontal Néel vector orientation. The data is collected at 5 K. **e-f**, SHG intensity as a function of temperature of the as-exfoliated (**e**) and strained (**f**) sample after one thermal cycle. The difference of the Néel temperature is within 1 K.

Supplementary Information for “Imaging the Néel vector switching in the monolayer antiferromagnet MnPSe₃ with strain-controlled Ising order”

Supplementary Note 1. Symmetry analysis of SHG responses

Above the Néel temperature T_N , the bulk MnPSe₃ has rhombohedral (ABC) stacking and belongs to the point group $\bar{3}$ (S_6) and the space group 148, where all of the mirror symmetries are broken, but the threefold rotation symmetry along the c axis and the inversion symmetry are present [1]. Below T_N , the material forms Néel AFM order, which breaks the inversion symmetry and the threefold rotation symmetry and allows all of the 18 non-zero terms in $\chi_{ijk}^{(2)}$.

Here we consider two sources contributing to the SHG signal: an electric-quadrupole (EQ) contribution from the lattice $P_i^{EQ}(2\omega) = \sum_{jkl} \chi_{ijkl}^{EQ} E_j \nabla_k E_l$ and an electric dipole (ED) contribution related with Néel vector (\mathbf{L}), $P_i^{ED}(2\omega) = \sum_{jk} \chi_{ijk}^{(2)}(\mathbf{L}) E_j E_k$. $\chi_{ijk}^{(2)}(\mathbf{L})$ generally depends on the Néel vector (\mathbf{L}). The EQ contribution is present at all temperature while the ED one is only allowed below T_N .

A. Electric-quadrupole contribution

First, we consider EQ contribution $P_i^{EQ}(2\omega) = \sum_{jkl} \chi_{ijkl}^{EQ} E_j \nabla_k E_l$. For a normally incident beam on the xy plane, we have $E_z = 0$ and $\nabla_x e^{iq_z z} = \nabla_y e^{iq_z z} = 0$. The point group symmetry allows eight non-zero elements with two independent values, $\chi_{xxxx}^{EQ} = -\chi_{yyzz}^{EQ} = -\chi_{yzyz}^{EQ} = -\chi_{xyzy}^{EQ}$ and $\chi_{yxxz}^{EQ} = \chi_{xxzy}^{EQ} = \chi_{yzxz}^{EQ} = -\chi_{yyzy}^{EQ}$. Assuming the polarization of incident light is at an angle of ϕ with respect to the a axis, we have $E = (\cos \phi, \sin \phi, 0)$. For parallel and crossed patterns, the detected polarization is along $(\cos \phi, \sin \phi, 0)$ and $(-\sin \phi, \cos \phi, 0)$, respectively. Therefore, the SHG intensity above Néel temperature is

$$I_{parallel}(2\omega, \phi) \propto q_z^2 |\chi_{xxxx}^{EQ} \cos 3\phi + \chi_{yxxz}^{EQ} \sin 3\phi|^2, \quad (S1)$$

$$I_{crossed}(2\omega, \phi) \propto q_z^2 |\chi_{xxxx}^{EQ} \sin 3\phi - \chi_{yxxz}^{EQ} \cos 3\phi|^2. \quad (S2)$$

Both of them are sixfold rotationally symmetric with the same amplitude, and peak positions are dependent on the ratio of χ_{xxxx}^{EQ} and χ_{yxxz}^{EQ} . A fit to SHG data at 100 K in a 100-nm thick MnPSe₃ sample is shown in Fig. 1b in the main text. Note that in the fit there is a shift of the angle by a constant set by the angle between the lab axis and the crystal a axis.

B. Electric-dipole contribution from the Néel AFM order

Next, we consider the ED contribution $P_i^{ED}(2\omega) = \sum_{jk} \chi_{ijk}^{(2)}(\mathbf{L}) E_j E_k$ related with the Néel vector \mathbf{L} . One could also write this term to relate with the Néel vector by $P_i^{ED}(2\omega) = \sum_{jkl} \chi_{ijkl}^{ED} E_j E_k L_l$, where $\chi_{ijk}^{(2)}(\mathbf{L}) = \sum_l \chi_{ijkl}^{ED} L_l$. Since all the non-zero $\chi_{ijkl}^{(2)}$ are allowed in the AFM ordered state, it is impractical to fit the polar patterns to extract the components. Under normal incidence, there are still six non-zero independent terms in the ordered phase.

Consider that the crossed polar patterns from monolayer to bulk are quite similar at all temperature below the transition temperature, to derive a simpler relationship with the Néel vector, we use a Taylor expansion at $\mathbf{L} = 0$ (near the phase transition) to expand $\chi_{ijk}^{(2)}$ up to the linear term,

$$\chi_{ijk}^{(2)}(\mathbf{L}) = \sum_l \frac{\partial \chi_{ijk}^{(2)}}{\partial L_l} L_l |_{\mathbf{L}=0}. \quad (S3)$$

Then one can define a 4th-rank tensor $\chi_{ijkl}^N = \frac{\partial \chi_{ijk}^{(2)}}{\partial L_l} |_{\mathbf{L}=0}$ and the ED term is written as $P_i^N(2\omega) = \sum_{jkl} \chi_{ijkl}^N E_j E_k L_l$. Note that the Néel vector behaves the same as an electric field under the threefold rotation operation, the inversion operation, and the reflection operation vertical to the a axis in the lattice of MnPSe₃. The former two are the symmetry operations in the lattice of a multi-layer MnPSe₃ while the last one is an additional symmetry operation in

the lattice of the monolayer MnPSe₃ with the spins along the a axis. Therefore, we could treat the Néel vector similar to an electric field in the symmetry analysis. The tensor χ_{ijkl}^N has the lattice symmetry in paramagnetic phase. The non-zero components of the ED SHG susceptibility tensor in the ordered state could be derived from the symmetries of the susceptibility tensor in the high-temperature phase and the order parameter [2], $\chi_{ijk}^N = \sum_{kl} \chi_{ijkl}^N L_l$, where L_l is a component of the Néel vector. Note that the symmetry of χ_{ijkl}^N is higher than the general χ_{ijkl}^{ED} that applies to the temperature below T_N because we only consider up to the linear order in Equa. S3. Therefore, χ_{ijkl}^N applies to the temperature near the phase transition and could be extended to the general ED SHG susceptibility tensor by considering higher-order terms. Note that the discussion in this paragraph applies to monolayer and bulk samples.

Monolayer MnPSe₃ has a mirror symmetry along ac plane and a threefold rotation symmetry along c axis without the AFM order. With the lattice symmetry and the exchange symmetry of indices k and l , one can write the tensor to be

$$\left(\begin{pmatrix} \chi_{xxxx}^N & 0 \\ 0 & \frac{1}{2}(\chi_{xxxx}^N - \chi_{yyyy}^N) \\ 0 & \chi_{xyyx}^N \\ \frac{1}{2}(\chi_{xxxx}^N - \chi_{xyyx}^N) & 0 \end{pmatrix} \begin{pmatrix} 0 & \frac{1}{2}(\chi_{xxxx}^N - \chi_{xyyx}^N) \\ \chi_{xyyx}^N & 0 \\ \frac{1}{2}(\chi_{xxxx}^N - \chi_{xyyx}^N) & 0 \\ 0 & \chi_{xxxx}^N \end{pmatrix} \right). \quad (S4)$$

To calculate polarization dependent SHG signal, we define ϕ to be the angle of incident light polarization and θ to be the angle of the Néel vector with respect to the a axis. Therefore $E = (\cos \phi, \sin \phi, 0)$ and $L = (\cos \theta, \sin \theta, 0)$. Eventually one gets

$$I_{parallel}(2\omega, \phi) \propto L^2 |\chi_{xxxx}^N \cos(\phi - \theta)|^2, \quad (S5)$$

$$I_{crossed}(2\omega, \phi) \propto L^2 |\chi_{xyyx}^N \sin(\phi - \theta)|^2. \quad (S6)$$

These results enable us to identify the direction of Néel vector. It is interesting to note that only the orientation but not the shape and magnitude of ED-SHG patterns would change when the direction of Néel vector changes.

Layer stacking in multi-layer MnPSe₃ breaks the mirror symmetry while maintain the threefold rotation symmetry in lattice. Therefore more tensor elements need to be considered. The new tensor is

$$\left(\begin{pmatrix} \chi_{xxxx}^N & -\chi_{xxxy}^N \\ -\frac{1}{2}(\chi_{xxxy}^N + \chi_{yxxx}^N) & \frac{1}{2}(\chi_{xxxx}^N - \chi_{xyyx}^N) \\ \chi_{yxxx}^N & \chi_{xyyx}^N \\ \frac{1}{2}(\chi_{xxxx}^N - \chi_{xyyx}^N) & \frac{1}{2}(\chi_{xxxy}^N + \chi_{yxxx}^N) \end{pmatrix} \begin{pmatrix} -\frac{1}{2}(\chi_{xxxy}^N + \chi_{yxxx}^N) & \frac{1}{2}(\chi_{xxxx}^N - \chi_{xyyx}^N) \\ \chi_{xyyx}^N & -\chi_{yxxx}^N \\ \frac{1}{2}(\chi_{xxxx}^N - \chi_{xyyx}^N) & \frac{1}{2}(\chi_{xxxy}^N + \chi_{yxxx}^N) \\ -\chi_{xxxy}^N & \chi_{xxxx}^N \end{pmatrix} \right). \quad (S7)$$

Considering a incident electric field $E_{in} = (\cos \phi, \sin \phi, 0)$ and Néel vector $L = (\cos \theta, \sin \theta, 0)$, the output second-order response is then

$$I_{parallel}(2\omega, \phi, \theta) \propto L^2 |\chi_{xxxx}^N \cos(\theta - \phi) + \chi_{xxxy}^N \sin(\theta - \phi)|^2, \quad (S8)$$

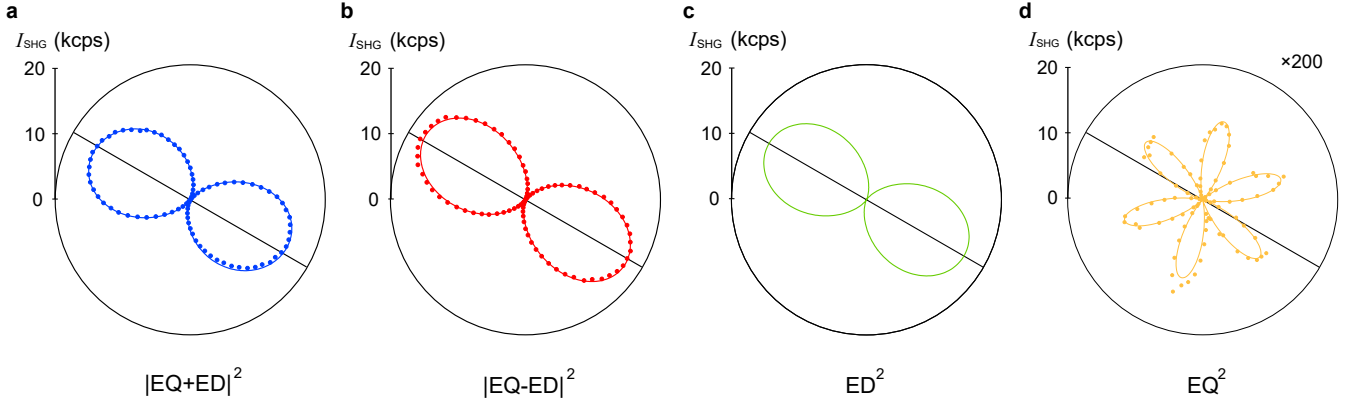
$$I_{crossed}(2\omega, \phi, \theta) \propto L^2 |\chi_{yxxx}^N \cos(\theta - \phi) + \chi_{xyyx}^N \sin(\theta - \phi)|^2. \quad (S9)$$

When the crossed pattern has a node (that crosses zero), according to our simulation, there are two possibilities: (1) χ_{yxxx}^N is much smaller than χ_{xyyx}^N ; (2) χ_{yxxx}^N and χ_{xyyx}^N are almost in phase. In the first case, the node direction in the across pattern is the Néel vector direction. In the second case, their direction are off by an angle of $\arctan \frac{|\chi_{yxxx}^N|}{|\chi_{xyyx}^N|}$.

To summarize, the crossed polar pattern could be described by $L^2 \sin(\theta - \phi + C)^2$, where C is a constant.

C. Coupling between ED and EQ terms

In our experiment, the in-plane uniaxial anisotropy caused by the strain pins the Néel vector to an Ising type. Therefore, the in-plane Néel vector can only switch between two opposite directions reversed by the time-reversal operation. If the SHG signal is purely from the ED contribution, there is no way to distinguish these two domains because of the lack of phase information in the SHG measurement. However, by interfering the ED contribution with



Supplementary Figure 1: A fit to crossed patterns in two Ising domains in the $\sim 15 \mu\text{m}$ thick MnPSe_3 bulk crystal in Fig. 2a-c in the main text. a, A crossed pattern of domain 1 at 5 K, b, a crossed pattern of domain 2 at 5 K. c, Extracted pure ED contribution from the fit. d, Crossed pattern multiplied by a factor of 200 at 100 K.

the EQ contribution, it is possible to get different responses from two domains even though the EQ term is much smaller than the ED term. The total SHG intensity is

$$I_{\text{parallel}}^{\text{total}} = \left| L\chi_{xxxx}^N \cos(\theta - \phi) + L\chi_{xxyy}^N \sin(\theta - \phi) + q_z\chi_{xxzx}^{EQ} \sin 3\phi + q_z\chi_{yxxz}^{EQ} \sin 3\phi \right|^2, \quad (\text{S10})$$

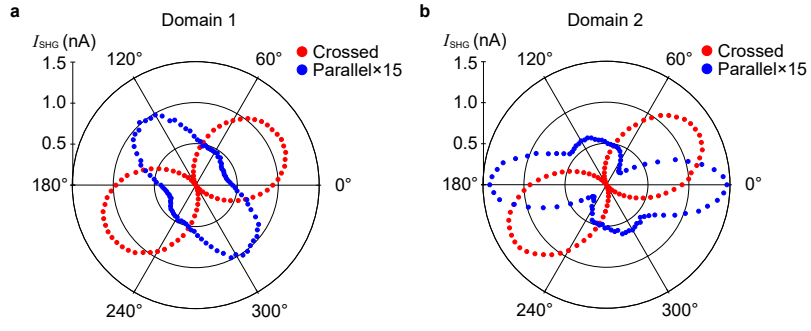
$$I_{\text{crossed}}^{\text{total}} = \left| -L\chi_{yxxx}^N \cos(\theta - \phi) - L\chi_{xyyx}^N \sin(\theta - \phi) + q_z\chi_{xxzx}^{EQ} \sin 3\phi - q_z\chi_{yxxz}^{EQ} \cos 3\phi \right|^2. \quad (\text{S11})$$

In the main text, we show the existence of two different crossed patterns corresponding to two Ising domains. To test whether the data are consistent with the above analysis, we fit two crossed patterns of two Ising domains from a $\sim 15 \mu\text{m}$ sample using Equa. (S11). Crossed polar patterns for domain 1 and 2 are plotted by blue and red dots in Supplementary Figure 1. Since the EQ term is not expected to change with temperature, we use the EQ term in the crossed pattern above Néel temperature. The crossed pattern measured at 100 K is shown by yellow dots in Supplementary Figure 1d. Note the 100 K pattern is magnified by 200 times. We fit the three curves simultaneously with the fitting weight of the 100 K data being 200 times larger than the other two at 5 K. The best fit results are shown in solid lines in Supplementary Figure 1. It matches well with all of the three patterns. The green and yellow solid lines represent the extracted pure ED and EQ contributions. In thick samples, the magnitude of the crossed pattern signal remains almost the same but with a small angle change in the node direction when domain change happens because of the much larger ED contribution than the EQ one. In thin samples, especially in the monolayer (see main text Fig. 3j), crossed patterns of two domains look more different in terms of the orientation, which results from a smaller ratio between ED term and EQ term.

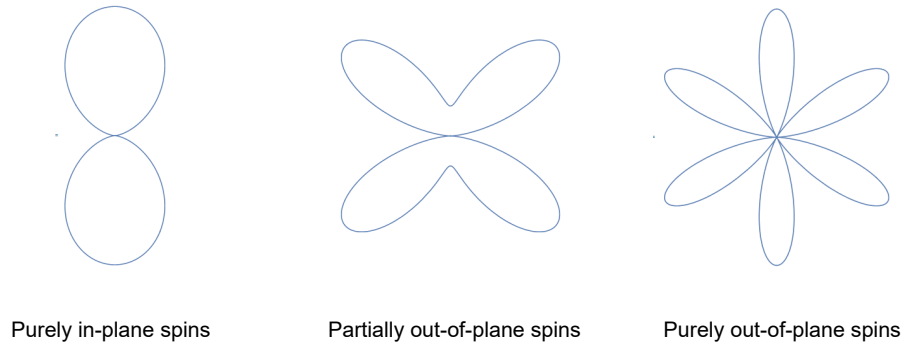
The ED term in the parallel configuration at 5 K is around 4–6 times larger than the EQ term above T_N (for example, see Supplementary Figure 4 on a $\sim 50 \text{ nm}$ sample.). It induces a significant change of the polar pattern when the Néel vector reverses. We have showed the switching of parallel polar patterns of a $\sim 15 \mu\text{m}$ thick, monolayer and bilayer samples. Here we show the domain switching in a $\sim 100 \text{ nm}$ thick sample and the polar patterns corresponding to two domains are shown in Supplementary Figure 2. Note that this is a 3rd 100 nm sample which is different from those in Fig. 1b and Fig. 2d-f in the main text.

D. SHG patterns in the existence of out-of-plane Néel vector component

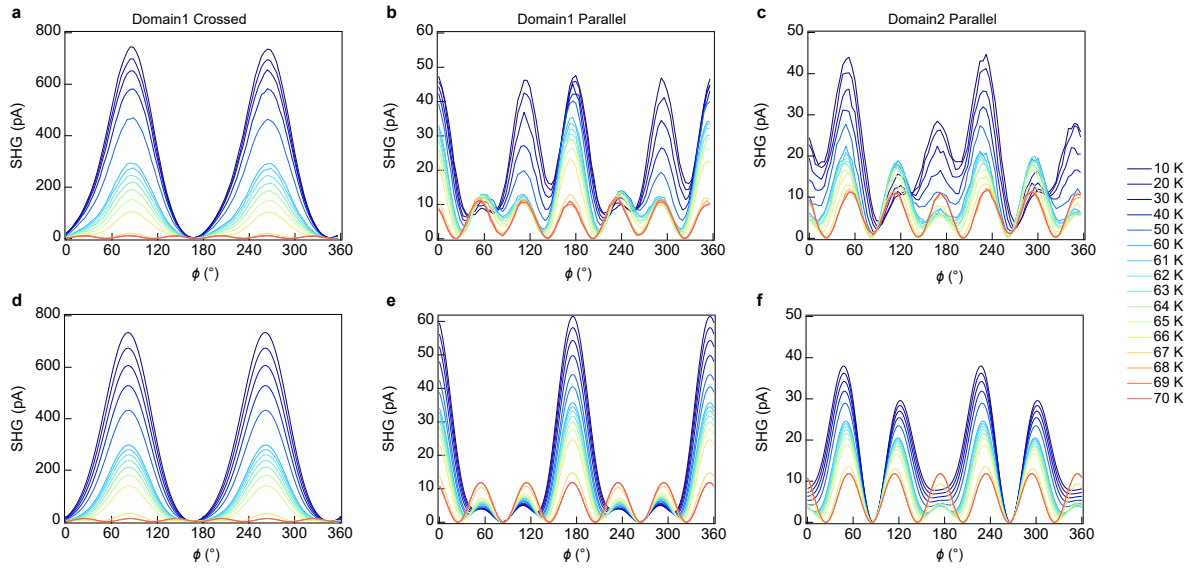
As discussed in the main text, the neutron scattering experiment reveals that spins in MnPSe_3 are in-plane [1]. From SHG patterns, one can also tell whether the spin direction is out-of-plane or in-plane. From Equa. S3 and Equa. S7, one can obtain a sixfold SHG patterns when \mathbf{L} has a pure z-component and twofold SHG patterns when \mathbf{L} has no z-component. When the \mathbf{L} has both in-plane and out-of-plane components, the SHG pattern is neither twofold nor sixfold patterns. Examples of crossed patterns in each case are shown in Supplementary Figure 3. Based on this analysis, the twofold crossed patterns we observe in the experiment also support the picture of in-plane Néel vector.



Supplementary Figure 2: Polar patterns in domain switching of a third ~ 100 nm flake on SiO_2/Si . a, Parallel and b, crossed polar patterns on two domains at 5 K.



Supplementary Figure 3: A comparison of crossed SHG patterns under purely in-plane, partially out-of-plane and purely out-of-plane spins.



Supplementary Figure 4: Temperature dependence of SHG patterns in an ~ 50 nm thick MnPSe_3 flake on SiO_2/Si . a, Crossed and b parallel patterns in domain 1. c Parallel patterns in domain 2. d-f Simulated crossed (d) and parallel (e) patterns in domain 1 and (f) parallel pattern in domain 2 by using Equa.S11 with $L = (1 - T/T_N)^\beta$.

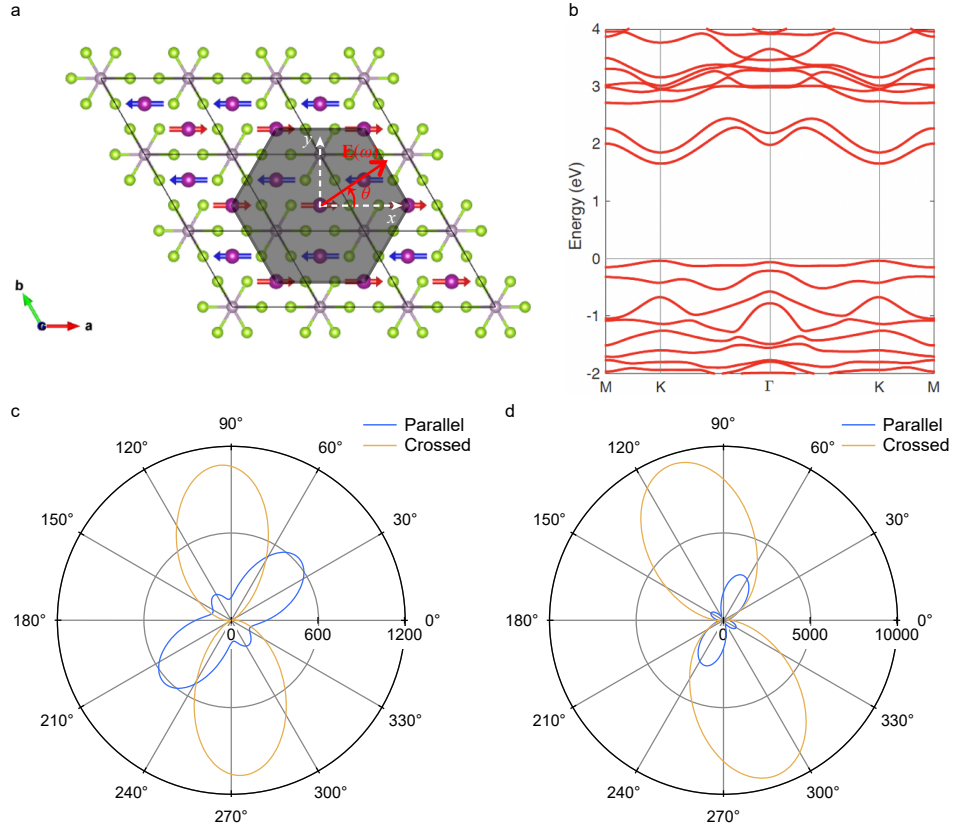
E. Temperature dependence of SHG patterns in a ~ 50 nm thick flake exfoliated on SiO_2/Si

Here we examine the validity of neglecting the higher-order terms in the Taylor expansion of second-order susceptibility. When the temperature is close enough to the Néel temperature, the Néel vector \mathbf{L} is small, and therefore, it is reasonable to neglect higher-order terms of \mathbf{L} . However, when the sample temperature is far below the Néel temperature, all of the 6 non-zero terms in second-order susceptibility $\chi^{(2)}$ are necessary. To test this, we measure the temperature dependence of SHG patterns at one spot of a ~ 50 nm thick flake. In Supplementary Figure 4a,b, we show the data for crossed and parallel patterns in domain 1 and in Supplementary Figure 4c, we show the parallel pattern for domain 2. Using Equa.S10 and S11 we perform a simulation of the experiment data with $L = (1 - T/T_N)^\beta$ (shown in Supplementary Figure 4d-f). The experiment and simulation match well across the whole temperature in crossed patterns. In parallel patterns, however, the simulation using Equa. S10 matches the experiment near Néel temperature: in both domains 1 and 2, the experimental data is reproduced by the simulation above 60 K, but not captured well below 50 K. We also test a 4th 100-nm sample and reached the same conclusion that Equa. S10 works above 60 K. The break-down in parallel pattern indicates other χ_{ijk}^{ED} terms should be considered at low temperature, while for the crossed pattern, Equa. S11 is good enough to capture the key factors such as the amplitude and the node direction.

Supplementary Note 2. DFT calculation of the polar pattern from ED contribution

To see how the polar pattern looks like by considering all of the non-zero terms, we performed density functional theory calculation. Electronic structure of antiferromagnetically ordered monolayer MnPSe_3 with spin polarization aligned along x direction (a axis) shown in Supplementary Figure 5a. was calculated using first-principles density-functional theory (DFT) implemented in the Vienna *ab-initio* Simulation Package with a plane-wave basis and the projector-augmented wave method. We adopted the Perdew-Burke-Ernzerhof (PBE)'s form of exchange-correlation functional within the generalized-gradient approximation (GGA) and a Monkhorst-Pack k-point sampling for the Brillouin zone (BZ) integration. An energy cutoff of 300 eV for the plane-wave basis and a Monkhorst-Pack k-point sampling of $24 \times 24 \times 1$ were applied. Spin-orbit coupling was taken into account at the full-relativistic level. Hubbard U correction was included in the DFT-PBE calculations with $U_{eff} = U - J = 3.9$ eV to account for the correlation effect from $3d$ transition metal. The monolayer structure was extracted from the experimental bulk structure [1] which holds in-plane antiferromagnetically-ordered monolayer MnPSe_3 with spin polarization aligned along x direction (AFM-x, see Supplementary Figure 5a). The electronic band structure and spin density along x were shown in Supplementary Figure 5b. The calculated band-gap is ~ 1.6 eV, which was smaller than the experiment value 2.32 eV measured on a bulk sample [3] as expected for PBE+ U . Our room temperature optical conductivity measurement shown in Figure 11 is qualitatively the same as the previous work [3]. Moreover, the spin density is localized around Mn atoms with spin polarization along x axis. Note that the calculation does not take the exciton effect into consideration.

The magnetic point group of multi-layer (with the Néel vector along a axis) is $\bar{1}'$; hence the parity-time-symmetry allows c-type SHG with all components being symmetry allowed. SHG susceptibility tensor was calculated by using an in-house developed first-principles nonlinear optics package (iNLO)[4, 5] interfaced with VASP. Total 100 electronic bands were included in the calculations, and a small imaginary smearing factor of 0.05 eV was included in the fundamental frequency in the denominator of susceptibility tensor. The result at the incident photon energy of 0.83 eV is shown in Supplementary Figure 5c, considering that the gap size in the calculation is smaller by 0.73 eV and the incident photon energy in the experiment is centered at 1.55 eV. The anisotropy plot indicates that the lobes in the crossed pattern are mainly pointing perpendicular to the direction of the Néel vector. In other words, the node direction in the crossed pattern is close to the Néel vector direction, which supports the above analysis in Supplementary Note 1. We also point out that we looked at the node direction over a wide energy range from 0.6 eV to 1.2 eV for the incident photon energy in the calculation. It is always within $\sim 30^\circ$ from the Néel vector. An example of the polar patterns at 1.1 eV is shown in Supplementary Figure 5d, which also looks quite similar to the experiment.



Supplementary Figure 5: DFT results. **a**, Crystal structure of monolayer MnPSe₃ with AFM-x magnetic ordering. **b**, Electronic band structure of AFM-x MnPSe₃. **c-d**, Calculated parallel (blue) and crossed (gold) polar patterns at the incident photon energy of (c), 0.83 eV and (d), 1.1 eV.

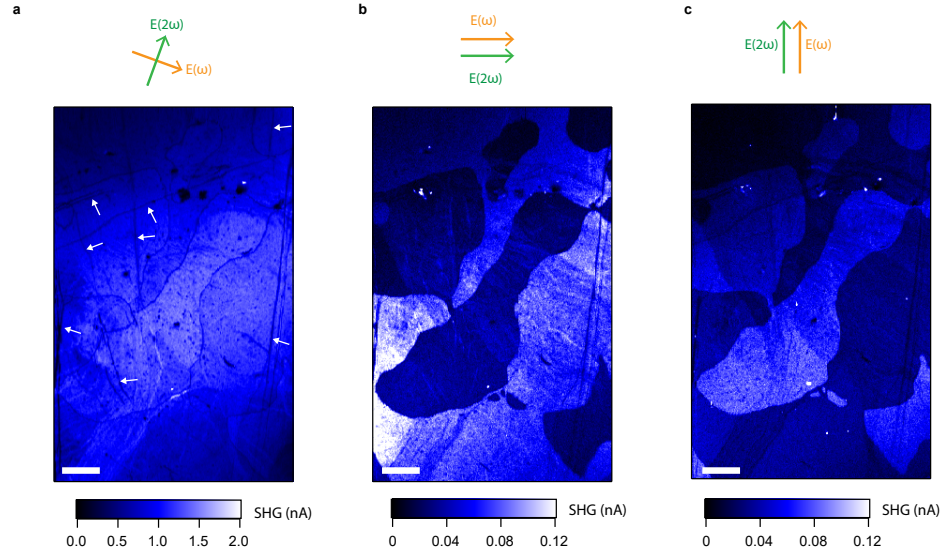
Supplementary Note 3. More SHG data

A. More SHG imaging about AFM domains on a bulk crystal

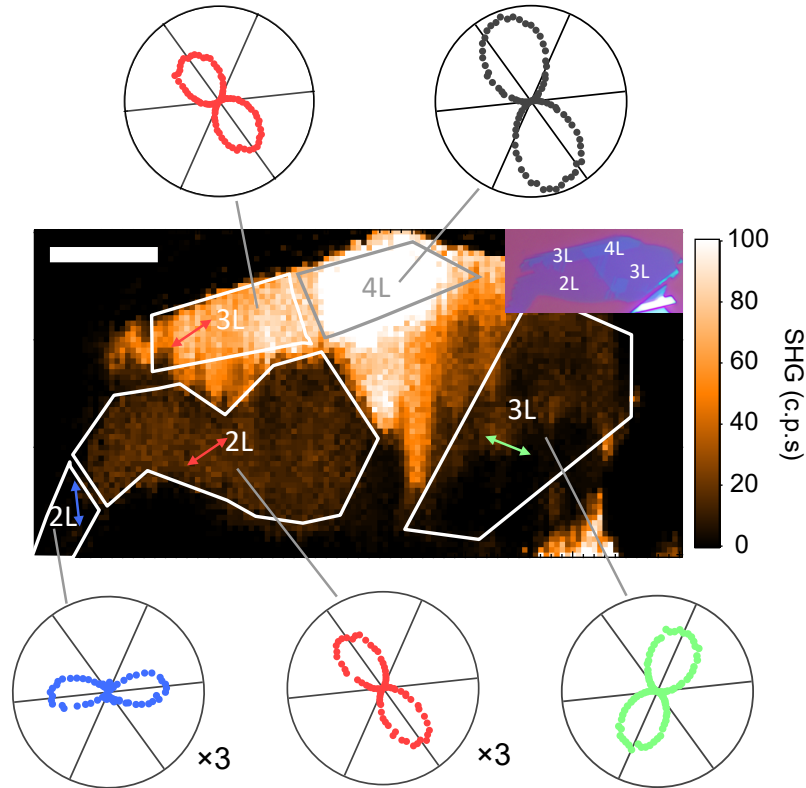
Here we show SHG mapping about AFM domains on a $\sim 30 \mu\text{m}$ bulk crystal in Supplementary Figure 6. The incident and detecting light polarization are shown on the top of each figure. Supplementary Figure 6a. is measured when the peak of the crossed pattern is reached. The darker lines indicated by the white arrows are scratches on the sample surface, while other darker lines indicate the AFM domain walls between 180° domains. Supplementary Figure 6b,c. show SHG intensity mapping in the parallel channel with two different polarizer angles. Two different domains are clearly distinguishable by different SHG intensity in both mappings with sharp contrasts. The outlines of the domains in the three figures match well. These observations are consistent with our previous discussion on the domain wall between two Ising domains.

B. SHG polar patterns and mapping on atomically thin few-layer MnPSe₃

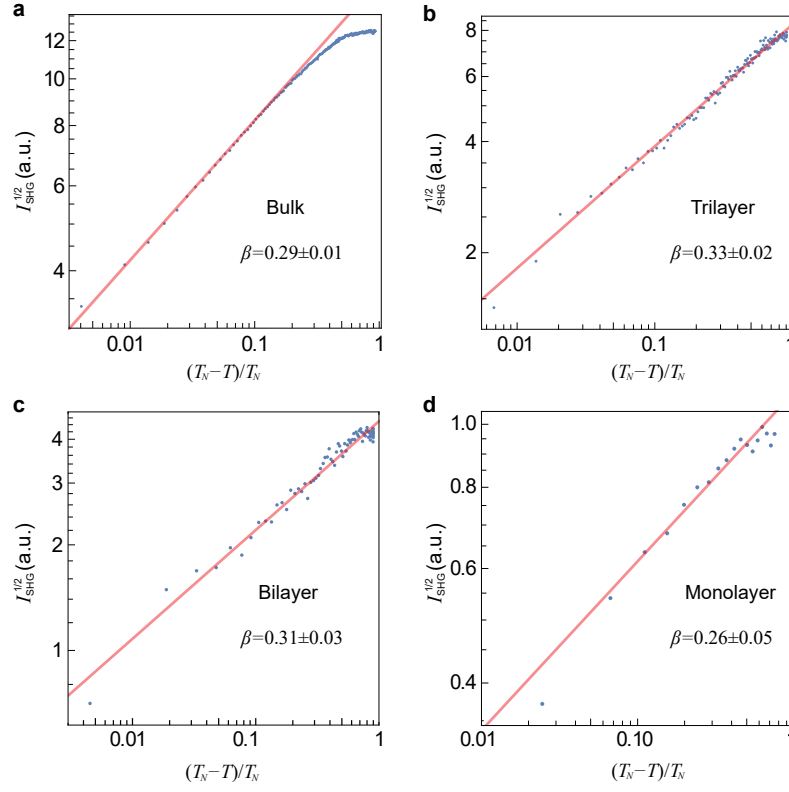
Supplementary Figure 7 shows an SHG intensity mapping in a multi-layer sample with different domains. The measuring polarization is chosen to be near the peak of areas marked by the red arrow. Regions with homogeneous thickness and same AFM domains are outlined by white lines (and gray line for the 4-layer sample). The arrows indicate the node direction in the crossed patterns. In each region, the crossed polar pattern is measured and shown beside the intensity mapping. Note that part of the 2L sample with the tail shape on the bottom left corner has a different Néel vector direction probably due to a different strain direction. Nevertheless, as we mentioned in the main text, all of the samples measured in this work, including these few-layer ones, all show two-state (Ising) ground state with in-plane spins across thermal cycles at randomly selected positions we measure.



Supplementary Figure 6: SHG intensity mapping in crossed and parallel configurations of a MnPSe_3 bulk crystal ($\sim 30 \mu\text{m}$ thick) at 5 K. **a**, Mapping with polarizers at the peak of the crossed pattern. The dark lines marked by white arrows are scratches on the sample surface. The dark lines without white arrows are mobile AFM domain walls. **b**, Mapping with polarizers at the peak of the parallel pattern in one of the domains. **c**, Mapping with polarizers at the peak of the parallel pattern of the other domain. Scale bar: $50 \mu\text{m}$. The incident and detecting polarization are marked by orange and green arrows, respectively.



Supplementary Figure 7: Néel vector mapping of an atomically thin multilayer MnPSe_3 sample exfoliated on the SiO_2/Si substrate in air. SHG intensity mapping of a MnPSe_3 flake with various layers. Areas with the same thickness and Néel vector direction are noted by the solid lines and labeled with the layer number. An optical image of the same flake is shown in the corner. The two-way arrows in different colors denote the node orientation (Néel vector direction) of the crossed pattern in the marked area. The measurement is performed at 5 K. Scale bar: $10 \mu\text{m}$.



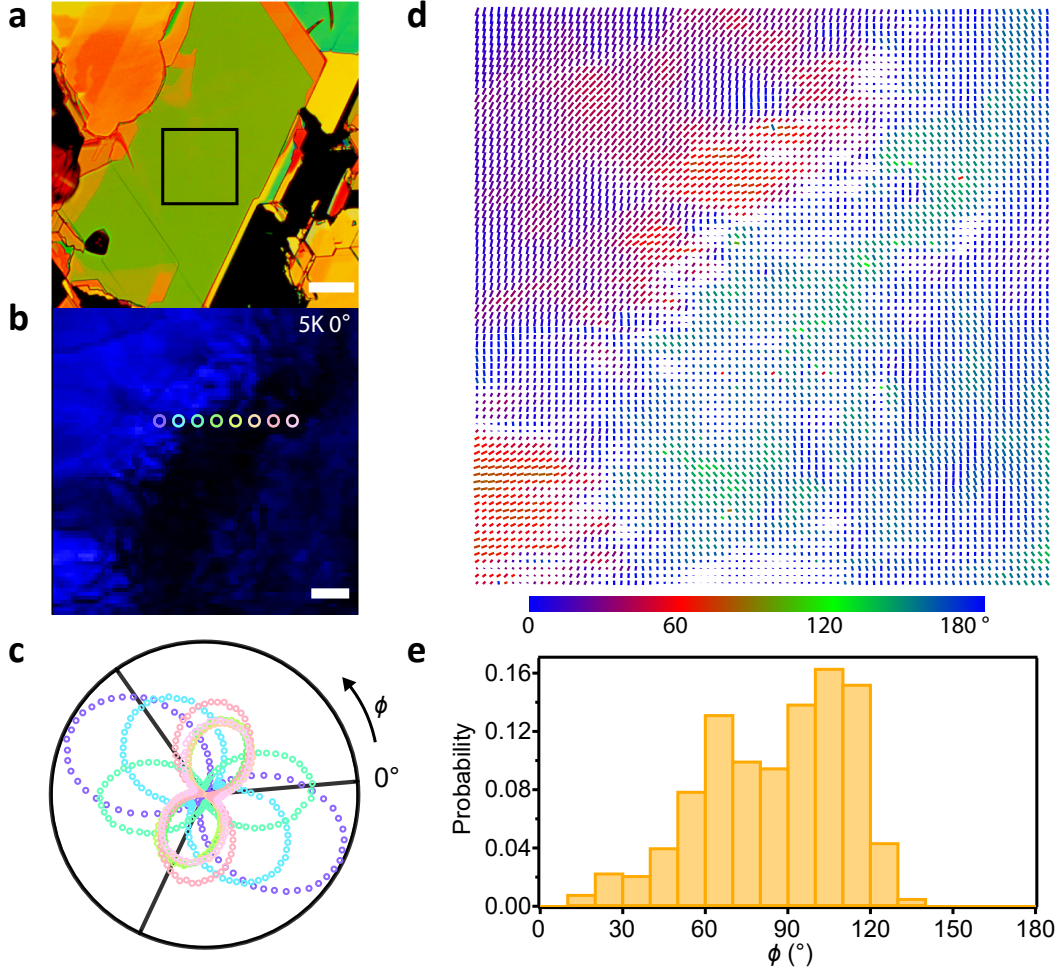
Supplementary Figure 8: Critical behaviors of MnPSe₃ samples shown in extended data Fig. 5. The temperature dependence of SHG intensity is shown in log-log plot. A linear fit to the data is applied to the linear region of each curves. **a**, 15 μm thick bulk. **b**, Trilayer. **c**, Bilayer. **d**, Monolayer. Few-layer samples in **b-d** are exfoliated in air.

C. Critical behavior fitting

The order parameter follows $(1 - T/T_N)^\beta$ with β being the critical exponent in a continuous phase transition. Since χ^{ED} is proportional to the order parameter [2], one can get $I_{SHG}^{1/2} \propto (1 - T/T_N)^\beta + b$ where b is a constant coming from the EQ contribution. In Supplementary Figure 8, we plot $(I_{SHG}^{1/2} - b)$ that was shown in Extended Data Figure 5 as a function of $(T_N - T)/T_N$ in a log-log plot. The slope of the linear curve near the origin is the critical exponent β . The experiment data and the best fit of bulk (a), trilayer (b), bilayer (c) and monolayer (d) samples are showed. Note the fitting error is pretty high in monolayer due to the uncertainty of the Néel temperature. Overall, the critical exponent is ~ 0.3 , and the critical exponent of $0.29 (\pm 0.01)$ in the 15 μm thick bulk crystal is most reliable considering the very dense temperature step in the measurement and the highest signal-to-noise ratio. From the critical component itself, even though it is close to the 3D Ising model ($\beta = 0.3265$) than the 3D XY model ($\beta = 0.348$), it is not very obvious that the phase transition belongs to the Ising universality class since the difference in β is small. Nevertheless, the collapse of the temperature-dependent SHG on two curves is a strong evidence for the Ising order.

D. Néel vector distribution in multi-layer MnPSe₃

Since the crossed pattern nodes are locked to the Néel vectors, it is possible to map the spatial distribution of Néel vector within a MnPSe₃ flake. To perform Néel vector mapping on thick flakes of MnPSe₃, a flat area of a $80 \mu\text{m} \times 80 \mu\text{m}$ on a 100-nm MnPSe₃ flake is chosen as indicated by the black square in Supplementary Figure 9a. Contrary to the uniform image under an optical microscope (Supplementary Figure 9a), the SHG signal, however, is highly inhomogeneous in this area (Supplementary Figure 9b). First, we measure the crossed patterns in the selected points marked with white circles in Supplementary Figure 9b. Both the magnitude and the orientation of Néel vectors are non-uniform revealed by crossed patterns shown in Supplementary Figure 9c. To map the crossed patterns in the whole region, we measured the crossed polar patterns in each spot with a $2 \mu\text{m}$ size and fit them by $L^2 \sin^2(\theta - \phi)$ to get the direction of the Néel vectors first. The lines in 9d represent the spatial distribution of the extracted directions



Supplementary Figure 9: Distribution of Néel vectors in a (fourth) as-exfoliated 100 nm thick MnPSe₃ flake on the SiO₂/Si substrate. **a**, Optical image of the flake. The green area in the center has a homogeneous thickness of around 100 nm. Scale bar: 50 μm . **b**, SHG intensity image of the squared area in **a** with polarizers at 0° of the crossed pattern. The measured area is 80 μm \times 80 μm . Scale bar: 10 μm . **c**, Crossed patterns in varying points. The position where patterns are taken are marked in **b**. **d**, Vector mapping of Néel vectors in the same area as **b**. The orientation of each line segment denotes the direction of the Néel vectors. Different orientations are marked by different colors. **e**, Histogram of orientations in **d**. The measurement is performed at 5 K.

of the Néel vectors. The directions of the node in crossed patterns are shown by the orientation of the line as well as the color of the line segments. Supplementary Figure 9e shows the histogram of the orientations of Néel vectors.

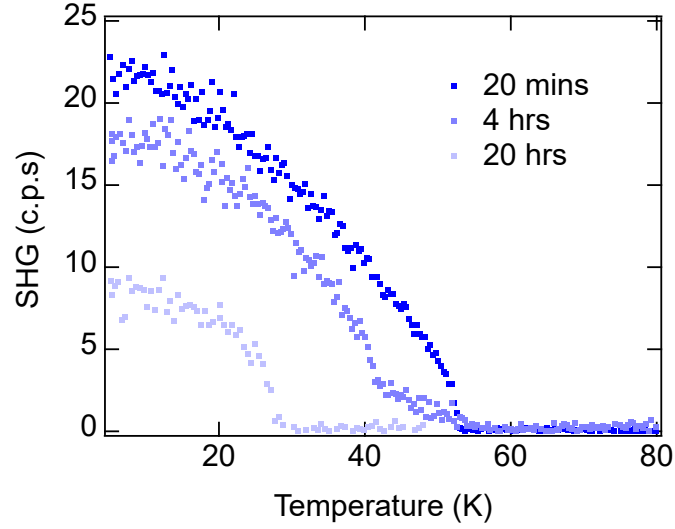
According to our previous analysis, the magnitude of the crossed pattern should not change if the direction of Néel vector changes in an unstrained thick flake. However, the L^2 from the fit shows the magnitude of crossed patterns is usually not the same at different positions. The magnitude of the Néel vector is represented by the length of the line segments. To resolve this inconsistency, we hypothesize that the orientation of the Néel vector could be different in different layers, probably due to the weak interlayer coupling.

We consider a multi-layer sample consisting of a few layers in a domain where the node direction of the crossed pattern points to $\theta = 0^\circ$ and another few layers with the node direction pointed along $\theta = 120^\circ$. For simplify we assume each layer produces same second-harmonic electric field. Then we can derive the total SHG signal in crossed pattern detected with incident polarization ϕ to be

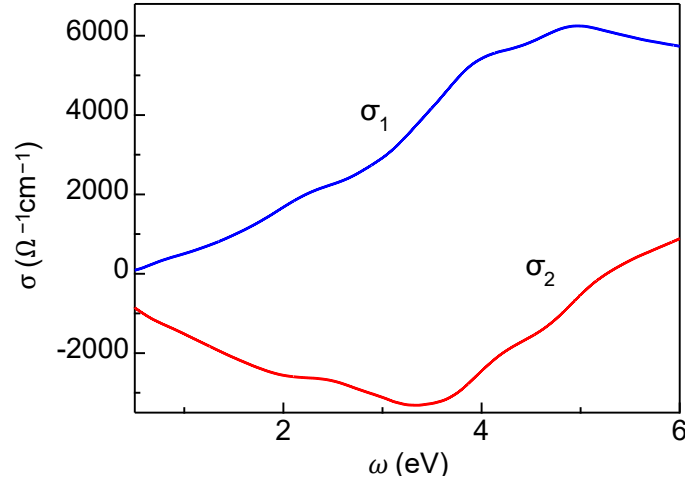
$$I_{crossed}^{total} \propto \left(A \sin \Delta\theta + B \sin \left(\Delta\theta - \frac{2\pi}{3} \right) \right)^2 \quad (\text{S12})$$

$$\propto (\alpha \sin (\Delta\theta + \gamma))^2, \quad (\text{S13})$$

where $\Delta\theta = \phi - \theta$ and α and γ are constants determined by A and B. By tuning A and B, we can observe a crossed



Supplementary Figure 10: Aging effect of an as-exfoliated bilayer MnPSe_3 sample in air.



Supplementary Figure 11: Optical conductivity of a MnPSe_3 bulk crystal at room temperature.

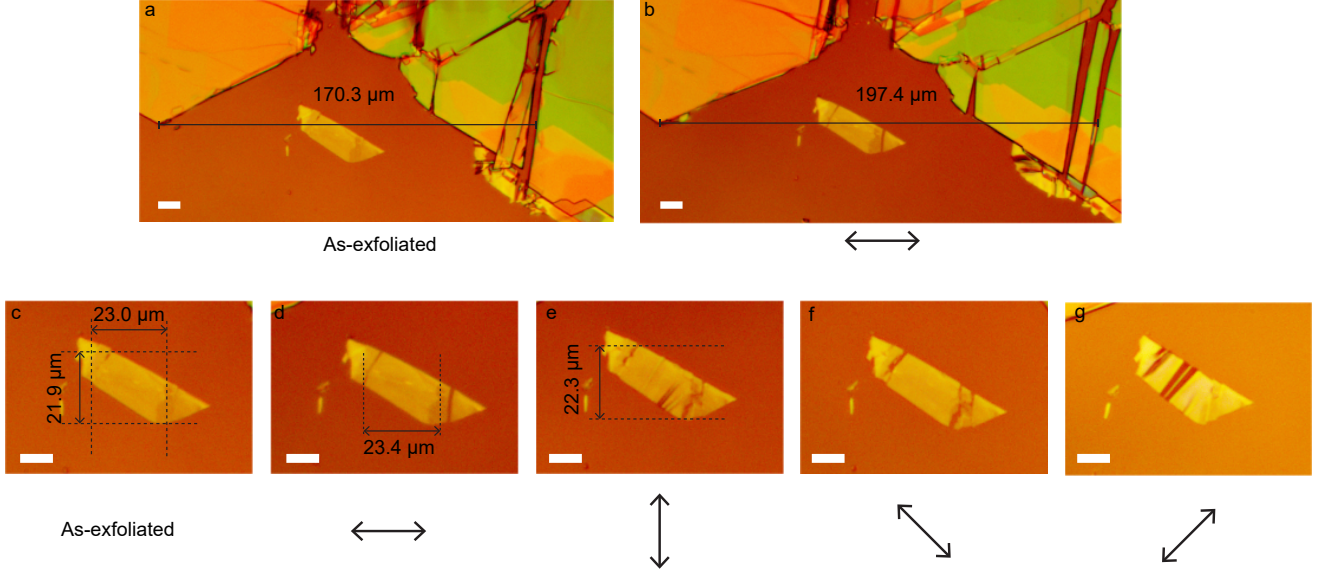
pattern with an arbitrary direction and amplitude for the Néel vector. Therefore, the experiment results in unstrained thick MnPSe_3 could be explained by contributions between different Néel vectors in different layers.

E. Aging effect of a bilayer MnPSe_3 sample in air

We tested the degradation of a bilayer MnPSe_3 by exposing it to air. We exposed the same sample in air for 20 mins, 4 hours, and 20 hours and measured the SHG intensity and the transition temperature. During each exposure, the sample was stored in an atmospheric environment with relative humidity less than 30%. With the increase of exposure time, the SHG intensity and the Néel temperature decrease (Supplementary Figure 10). We conclude that the MnPSe_3 is air-sensitive in its ultra-thin forms.

Supplementary Note 4. Strain dependent Néel vector distribution

First, we discuss how we determine the strain strength in MnPSe_3 flake and PDMS substrates. We show optical images of the strained sample presented in Fig. 4 in the main text. Images on the sample as-exfoliated and under uniaxial strain in four different directions are shown in Supplementary Figure 12. In each direction, a $\sim 15\%$ strain

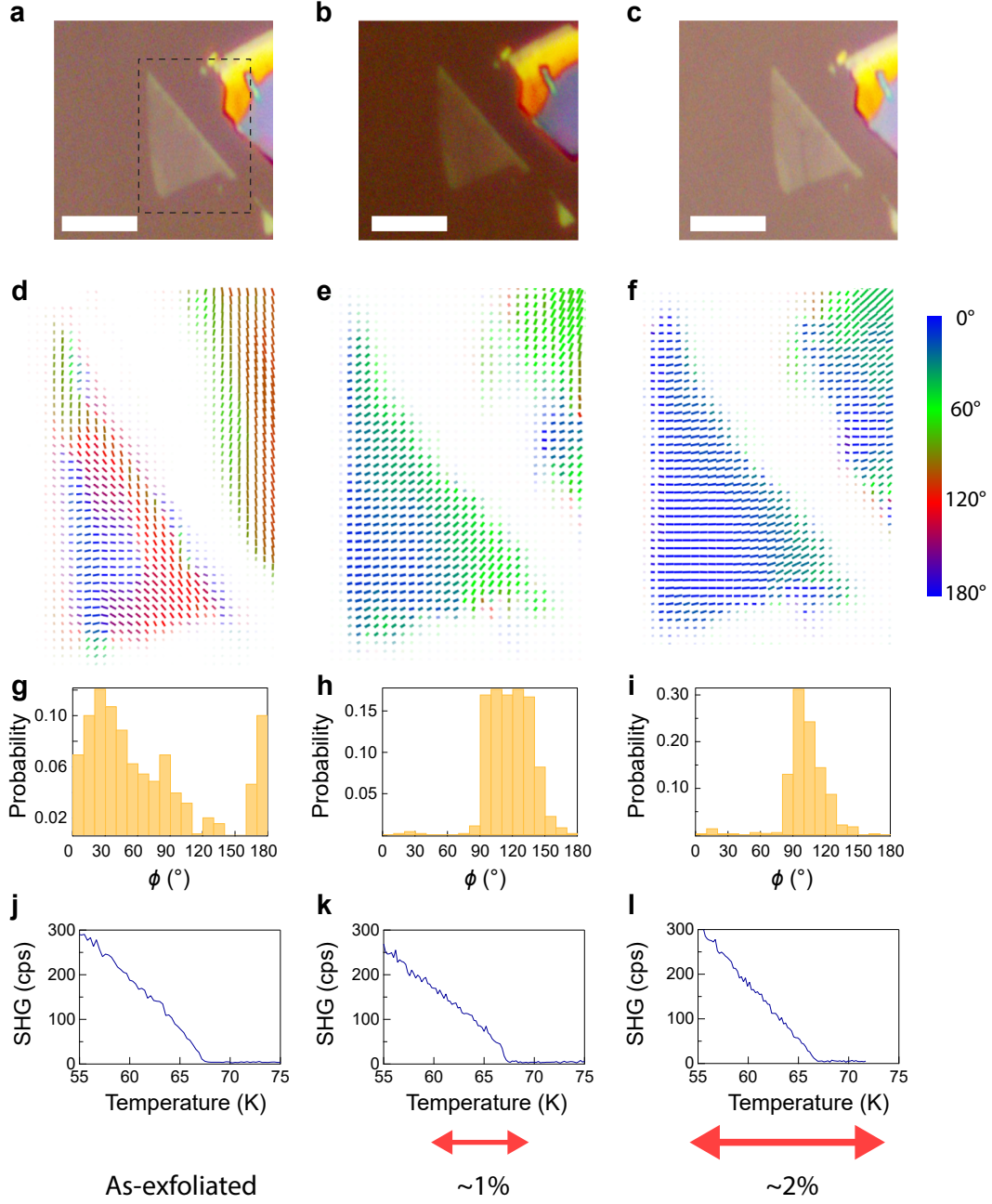


Supplementary Figure 12: Optical images of the MnPSe₃ sample in Fig.4 of the main text under strain. a-b, Optical image of the MnPSe₃ flake (~ 15 nm thick) on a PDMS substrate without being stretched (a) and a horizontally strained PDMS substrate (b). An elongation of 15-16% is observed by measuring the distance (solid line) between two bulk flakes. c-g, Optical images of the MnPSe₃ sample under strain in different directions. The two-way arrows beneath each image indicate the strain direction. A uniaxial $\sim 15\%$ strain is added to the PDMS substrate. A roughly $\sim 2\%$ strain is transferred onto the sample, which is estimated by measuring the sample length change in the optical images. Scale bar: 10 μm .

is added to the PDMS substrate by a micro-manipulator. Supplementary Figure 12a and b show the distance change between two bulk flakes (marked by the solid lines) before and after applying the strain, where elongation of 15-16% is observed in the strained substrate. We also made an estimation that around 2% strain is added to the sample by comparing the change of the length of the sample before and after adding the strain (shown in Supplementary Figure 12c-e). Note that the error bar is around $\pm 0.5\%$, and the strain strength on different sample positions is possible to be slightly different because of the finite sample size [6]. In Supplementary Figure 12d-g, optical images of the sample with different strain directions are shown. Nevertheless, as Fig. 4 in the main text shows that the SHG polar patterns are rotated and that the SHG intensity is uniform, strain is obviously added to the sample to align the Néel vectors. We hope that future Raman scattering experiments could determine the strain direction and strength more accurately. In our experimental, we could control strain direction within 10 degree, and the direction is more important. As shown in the microscopic spin model, small strain locks the Néel vector direction, and increasing the strain strength does not further tip the Néel vector in the linear response regime. Our SHG polar pattern measurement shows that the Néel vector is aligned towards the strain direction, and therefore, the conclusion of strain-controlled Ising order is valid even though the method of determining the strain strength by optical images (with cracks in the samples sometimes) might be less accurate than Raman scattering.

We investigate the effect of the strain on the Néel vector by applying different strength of strain along one direction on a MnPSe₃ flake with a thickness of 10 nm determined by atomic force microscopy measurement. The data are shown in Supplementary Figure 13. 7.5% and 15% strain are added to the PMDS substrate and the strain on the sample is estimated by the strain on the PMDS and a transfer ratio of 13%. When the sample is as-exfoliated and under 1% and 2% elongation, we map the node direction in the crossed patterns using the same method as described in Equa. S11. When the sample is as-exfoliated, the node directions do not point to a specific direction. When 1% strain is applied, the node direction in most regions points to the direction of the stretched direction except the region on the right edge. When we further add strain to 2%, the node direction points to the stretched direction across the whole sample. Note that because of the small sample size, the strain direction near the edge might be more influenced by the sample shape or the substrate during exfoliation process instead of the externally applied strain, which may explain the observation that it is harder to align the Néel vectors on the edges.

The PDMS substrate is not a good thermal conductor when it is 30 μm thick, and it can induce a ~ 10 K temperature difference between the sample and the platform, which is calibrated by measuring the transition temperature of a thick (> 50 nm) flake sample on the same PDMS substrate. We then measure the T_N with calibrated temperature



Supplementary Figure 13: Néel vector distribution in a 10-nm thick MnPSe_3 flake on a PDMS substrate under different strain strength. **a-c**, Optical image as-exfoliated, under 1% strain and 2% strain. The strain strength is estimated by the strain added to the PDMS times an estimated strain transfer rate of 13%. The sample thickness is measured by the atomic force microscopy. Scale bar: 10 μm . **d-f**, Néel vector (crossed pattern node) direction mapping at 5 K when the sample is as-exfoliated and under 1% strain and 2% strain. **g-i**, Histogram of the Néel vector (crossed pattern node) direction when the sample is as-exfoliated and under 1% strain and 2% strain. **j-l**, SHG intensity as a function of temperature when the sample is as-exfoliated and under 1% strain and 2% strain.

as shown in Supplementary Figure 13j-i. There is no observable T_N change (within 1 K) between these three cases.

Supplementary Note 5. Landau theory

Here we consider a Landau theory for the staggered magnetization M_i . Symmetries constrain the terms that can appear in the expansion. We have the rotationally invariant tensor δ_{ij} , which allows $|\vec{M}|^2$, and planar symmetry allows M_z^2 . We assume that this term is large, so that $M_z = 0$. For M in the xy plane, the 3-fold rotation symmetry, along with time reversal allows a term $(M_x + iM_y)^6 + c.c.$. This identifies an allowed rank 6 tensor that can be contracted with M_i .

Strain is described by a symmetric second rank tensor u_{ij} , whose principal axes describe the directions of compressive and tensile strain. To lowest order in the strain, a term $u_{ij}M_iM_j$ is allowed.

It is easiest to describe the magnetization in polar coordinates, $M_x + iM_y = Me^{i\theta}$. Then, the crystalline anisotropy gives $M^6 \cos 6\theta$. The symmetric strain can be diagonalized with a rotation about the c axis by an angle θ_0 . This term then gives $u_s M^2 \cos 2(\theta - \theta_0)$.

The Landau expansion (to lowest order in the coupling to strain) then takes the form

$$F = -atM^2 + bu_s M^2 \cos 2(\theta - \theta_0) + cM^4 + dM^6 + eM^6 \cos 6\theta \quad (\text{S14})$$

where $t = (T_c^0 - T)/T_c^0$. Here T_c^0 is the mean field critical temperature for $u_s = 0$. $M = L/2$, where L is the magnitude of the Néel vector.

Minimizing with respect to M and θ is equivalent to doing mean field theory. For $0 < t \ll 1$, this gives

$$M_0 = (at/2c)^{1/2} \quad (\text{S15})$$

with the mean field exponent $\beta = 1/2$.

For the critical behavior fluctuations are important and mean field theory breaks down. To get a better description of this, we can integrate out massive fluctuations in the magnitude M to obtain an effective theory for θ , which has the form,

$$F(\theta) = bu_s M_0^2 \cos 2(\theta - \theta_0) + eM_0^6 \cos 6\theta \quad (\text{S16})$$

As shown in main text Fig. 5, for $u_s = 0$ this reduces to the 6 state clock model. For $u_s \neq 0$ it is in the Ising universality class, and the antiferromagnetic order parameter is locked to the strain axis with a constant tilt angle.

Supplementary Note 6. Spin model

Here we construct a more microscopic spin model to explain the spin-strain locking. Space group 148 is a chiral group with the point symmetry C_3 . The high temperature state has two Mn sites on a honeycomb lattice. Below the Néel temperature the two sublattice sites develop different spin polarizations. Thus the AF transition is a condensation of two $\mathbf{G} = 0$ fields giving the spin polarizations on the α and β sublattice sites. Notice that this does not lower the translational symmetry of the structure, but only assigns the spins to the two sublattice sites.

The starting model for the structure has xy easy plane anisotropy. So the minimal model has on site anisotropy

$$\mathcal{H} = J \sum_{\text{nn: } \langle i \in \alpha, j \in \beta \rangle} \mathbf{s}_i \cdot \mathbf{s}_j + J_z \sum_{\forall i} (\mathbf{s}_i \cdot \hat{\mathbf{z}})^2$$

where $J > 0$ and $J_z > 0$.

Strain is a time reversal even, traceless second rank tensor $\varepsilon_{\mu\nu}$. Each link of the honeycomb lattice can be defined by an in-plane vector $\mathbf{d}_{ij} = \mathbf{r}_{(j \in \beta)} - \mathbf{r}_{(i \in \alpha)}$ and in the presence of strain we deform the links according to

$$\mathbf{d}_{ij} \mapsto \mathbf{d}_{ij} + \varepsilon \cdot \mathbf{d}_{ij}$$

In the following we are going to treat just the traceless part of ε which allows for deformation but not dilation or compression. The change of the exchange constants in any bond should be $\propto \varepsilon_{\mu\nu}$ but *even* under $\mathbf{d}_{ij} \mapsto -\mathbf{d}_{ij}$. We build the simplest model that does this. For any link define the unit vector $\hat{\mathbf{d}}_{ij}$ and the projections

$$\begin{aligned} \mathbf{s}_i \cdot \hat{\mathbf{d}}_{ij} & \quad , \quad \mathbf{s}_i - (\mathbf{s}_i \cdot \hat{\mathbf{d}}_{ij}) \hat{\mathbf{d}}_{ij} \\ \mathbf{s}_j \cdot \hat{\mathbf{d}}_{ij} & \quad , \quad \mathbf{s}_j - (\mathbf{s}_j \cdot \hat{\mathbf{d}}_{ij}) \hat{\mathbf{d}}_{ij} \end{aligned}$$

To lock the spin direction to the strain we have to replace the isotropic xy coupling in the original model by

$$J \mathbf{s}_i \cdot \mathbf{s}_j \mapsto J_{\parallel,ij} \mathbf{s}_{i,\parallel} \mathbf{s}_{j,\parallel} + J_{\perp,ij} \mathbf{s}_{i,\perp} \mathbf{s}_{j,\perp} + J_c (\mathbf{s}_{i,\parallel} \mathbf{s}_{j,\perp} + \mathbf{s}_{i,\perp} \mathbf{s}_{j,\parallel}) \quad (\text{S17})$$

distinguishing spin polarizations “along” and “perpendicular to” the ij -th link. If we keep the isotropic form of the nearest neighbor coupling it would exclude the possibility of any locking of the spin to the strain.

Combining the first two terms gives an expression like

$$J_{\perp} \mathbf{s}_i \cdot \mathbf{s}_j + (J_{\parallel} - J_{\perp}) (\mathbf{s}_i \cdot \hat{\mathbf{d}}_{ij}) (\mathbf{s}_j \cdot \hat{\mathbf{d}}_{ij})$$

so the first term just looks like the isotropic xy coupling and the spin-lattice locking comes from the second piece. To make this more transparent we notice that $i \in \alpha$ and $j \in \beta$, so in terms of the macroscopic spin fields \mathbf{S}_{α} and \mathbf{S}_{β} , it expresses as

$$J_{\perp} \mathbf{S}_{\alpha} \cdot \mathbf{S}_{\beta} + \mathbf{S}_{\alpha} \cdot \left[\sum_{\text{nn}:ij} \Delta J_{ij} \mathbf{d}_{ij} \otimes \mathbf{d}_{ij} \right] \cdot \mathbf{S}_{\beta}$$

where \otimes denotes the outer product, i.e. in component form $[\hat{\mathbf{d}} \otimes \hat{\mathbf{d}}]_{mn} = \hat{d}_m \hat{d}_n$. This contains an isotropic component that can be removed by explicitly writing this as an outer product

$$[\hat{\mathbf{d}} \otimes \hat{\mathbf{d}}]_{mn} = \left(\hat{d}_m \hat{d}_n - \frac{1}{2} \delta_{mn} \right) + \frac{1}{2} \delta_{mn}$$

This means that one must distinguish between the “longitudinal” and “transverse” spin couplings in any link but that the lattice sum produces an effective isotropic xy exchange constant $J = (J_{\parallel} + J_{\perp})/2$. The previous Landau expansion makes it clear that in the absence of strain the crystal field anisotropy can not appear at bilinear order in the spin Hamiltonian as indeed we find in this explicit model.

The above conclusion demonstrates that if the ΔJ ’s (which are symmetry allowed and therefore always present) were actually the *same* in each link then the traceless term in parenthesis gives zero after the sum over bonds because it is an $m = 2$ tensor averaged over a crystal with threefold rotational symmetry. Similarly, the lattice sum over the J_c term gives zero since the prefactors have the symmetry of an $m = 2$ tensor. However the trailing isotropic term gives a nonzero result after the lattice sum: $(J_{\parallel} - J_{\perp}) \mathbf{S}_{\alpha} \cdot \mathbf{S}_{\beta}/2$ and this contributes to the isotropic (xy) term of the spin Hamiltonian which then becomes

$$J \mathbf{S}_{\alpha} \cdot \mathbf{S}_{\beta} = \frac{J_{\perp} + J_{\parallel}}{2} \mathbf{S}_{\alpha} \cdot \mathbf{S}_{\beta}$$

The situation for the cross terms is similar. We can write the symmetric cross term in the exchange in the form

$$\begin{aligned} J_c [(\mathbf{s}_i \cdot \hat{\mathbf{d}})(\hat{\mathbf{z}} \cdot (\hat{\mathbf{d}} \times \mathbf{s}_j)) + (\hat{\mathbf{z}} \cdot (\hat{\mathbf{d}} \times \mathbf{s}_i))(\hat{\mathbf{d}} \cdot \mathbf{s}_j)] = \\ J_c [(\mathbf{s}_i \cdot \hat{\mathbf{d}})(\hat{\mathbf{z}} \times \hat{\mathbf{d}}) \cdot \mathbf{s}_j + (\mathbf{s}_i \cdot (\hat{\mathbf{z}} \times \hat{\mathbf{d}}))(\hat{\mathbf{d}} \cdot \mathbf{s}_j)] \end{aligned}$$

Using the notation $\hat{\mathbf{d}} = (\hat{d}_x, \hat{d}_y)$ it is useful to write this

$$J_c \mathbf{s}_i \cdot [\hat{\mathbf{d}} \otimes (\hat{\mathbf{z}} \times \hat{\mathbf{d}}) + (\hat{\mathbf{z}} \times \hat{\mathbf{d}}) \otimes \hat{\mathbf{d}}] \cdot \mathbf{s}_j$$

Explicitly, the quantity in brackets is

$$[\dots] = 2 \left[-\hat{d}_x \hat{d}_y \begin{pmatrix} 1 & 0 \\ 0 & -1 \end{pmatrix} + \frac{(d_x^2 - d_y^2)}{2} \begin{pmatrix} 0 & 1 \\ 1 & 0 \end{pmatrix} \right]$$

Because of the tensor character of the coefficients a *constant* value of J_c in each bond gives no contribution to the exchange coupling. In the absence of strain the lattice sum allows only the isotropic xy coupling.

Finally, the values of the exchange constants $(J_{\parallel} - J_{\perp})$ and J_c (both scalars) can vary in each link depending on the strain, and presumably one can linearize them in the manner

$$\begin{aligned} J_{\parallel,ij} - J_{\perp,ij} &= \Delta J_0 + \Delta J_1 (\hat{\mathbf{d}}_{ij} \cdot \boldsymbol{\varepsilon} \cdot \hat{\mathbf{d}}_{ij}) \\ J_{c,ij} &= J_c + \Delta J_{1,c} (\hat{\mathbf{d}}_{ij} \cdot \boldsymbol{\varepsilon} \cdot \hat{\mathbf{d}}_{ij}) \end{aligned}$$

where the subscript (1) denotes the coefficient of the linear term in the expansion in powers of the strain coupling. Then by combining all these expressions, we arrive at a result for longitudinal and transverse strain couplings we had previously

$$\Delta J_1 \left[\hat{\mathbf{d}}_{ij} \cdot \boldsymbol{\varepsilon} \cdot \hat{\mathbf{d}}_{ij} \right] \left(\mathbf{s}_i \cdot \hat{\mathbf{d}}_{ij} \right) \left(\mathbf{s}_j \cdot \hat{\mathbf{d}}_{ij} \right)$$

(Note that in this expression it is not necessary to explicitly remove the isotropic piece from the outer product because the summand includes only the traceless part of the strain tensor. In this case the lattice sum containing the ΔJ_1 factor does not affect isotropic spin coupling. If one were to restore the dilational strain the isotropic piece would then renormalize the effective isotropic J in the xy model). Rewriting this in terms of the macroscopic spin fields

$$J \mathbf{S}_\alpha \cdot \mathbf{S}_\beta + \Delta J_1 \mathbf{S}_\alpha \cdot \left(\sum_{\text{nn}: ij} \left[\hat{\mathbf{d}}_{ij} \cdot \boldsymbol{\varepsilon} \cdot \hat{\mathbf{d}}_{ij} \right] \hat{\mathbf{d}}_{ij} \otimes \hat{\mathbf{d}}_{ij} \right) \cdot \mathbf{S}_\beta$$

This last term has the requisite symmetries: it is even under $\mathbf{d} \mapsto -\mathbf{d}$ and $\propto \boldsymbol{\varepsilon}$ and is \mathcal{T} -even.

In the Néel state the moments on the two sublattices are collinear (antiparallel): $\mathbf{S}_\alpha = -\mathbf{S}_\beta = \mathbb{S}$, so one can rewrite this

$$-J |\mathbb{S}|^2 - \Delta J_1 \mathbb{S} \cdot \left(\sum_{\text{nn}: ij} \left[\hat{\mathbf{d}}_{ij} \cdot \boldsymbol{\varepsilon} \cdot \hat{\mathbf{d}}_{ij} \right] \hat{\mathbf{d}}_{ij} \otimes \hat{\mathbf{d}}_{ij} \right) \cdot \mathbb{S}. \quad (\text{S18})$$

In this expression $\boldsymbol{\varepsilon}$ is the externally imposed (traceless) strain and the sum is over a triad of nearest neighbor bonds away from an α sublattice site.

A similar analysis for the cross term allows for its variation as a function of strain, i.e. using the linearize piece $J_{c,1} \left(\hat{\mathbf{d}}_{ij} \cdot \boldsymbol{\varepsilon} \cdot \hat{\mathbf{d}}_{ij} \right)$ we get

$$-\Delta J_{c,1} \mathbb{S} \cdot \left(\sum_{\text{nn}: ij} \left[\hat{\mathbf{d}}_{ij} \cdot \boldsymbol{\varepsilon} \cdot \hat{\mathbf{d}}_{ij} \right] \left[\hat{\mathbf{d}}_{ij} \otimes (\hat{\mathbf{z}} \times \hat{\mathbf{d}}_{ij}) + (\hat{\mathbf{z}} \times \hat{\mathbf{d}}_{ij}) \otimes \hat{\mathbf{d}}_{ij} \right] \right) \cdot \mathbb{S}. \quad (\text{S19})$$

Summing equations 2 and 3 over a triad of bonds from an α site gives a 2×2 matrix parameterized by ΔJ_1 and $\Delta J_{c,1}$ whose principal axes denote the best and worst orientations of the Néel field in the presence of a strain $\boldsymbol{\varepsilon}$. Summing the second bracket from both equations gives a form

$$\hat{\mathbf{d}}_{ij} \otimes \left(\Delta J_1 \hat{\mathbf{d}}_{ij} + \Delta J_{c,1} (\hat{\mathbf{z}} \times \hat{\mathbf{d}}_{ij}) \right) + \left(\Delta J_1 \hat{\mathbf{d}}_{ij} + \Delta J_{c,1} (\hat{\mathbf{z}} \times \hat{\mathbf{d}}_{ij}) \right) \otimes \hat{\mathbf{d}}_{ij}$$

The terms proportional to ΔJ_1 try to align the Néel field along the strain axes, whereas the cross product terms tip the Néel with respect to $\boldsymbol{\varepsilon}$.

This can be seen most simply by carrying out the sum in a chiral basis where $S_\pm = S_x \pm iS_y$. If the principle axis of the strain tensor is aligned at angle θ_o one finds that the lattice sum gives an anisotropic spin coupling expressed as a matrix

$$\begin{aligned} & \begin{pmatrix} S_- & S_+ \end{pmatrix} \begin{pmatrix} 0 & (\Delta J_1 + i\Delta J_{c,1})e^{2i\theta_o} \\ (\Delta J_1 - i\Delta J_{c,1})e^{-2i\theta_o} & 0 \end{pmatrix} \begin{pmatrix} S_+ \\ S_- \end{pmatrix} \\ &= |\Delta J| \left[(S_x - iS_y)^2 e^{i(2\theta_o + \alpha)} + (S_x + iS_y)^2 e^{-i(2\theta_o + \alpha)} \right] \\ &= 2|\Delta J| |S|^2 \cos(2(\theta - \theta_o - \alpha/2)) \end{aligned}$$

where $|\Delta J| = \sqrt{\Delta J_1^2 + \Delta J_{c,1}^2}$ and $\alpha = \arctan[\Delta J_{c,1}/\Delta J_1]$ defines a misalignment angle of the spin orientation θ . This shows that the role of the strain coupling is to source two units of angular momentum in the spin Hamiltonian and that if we ignore the cross-coupling term the Néel vector would have a favored alignment along a principal axis of the strain tensor. The cross-coupling term is symmetry allowed and it misaligns the Néel field. The amount of this misalignment, which determines the direction of the Néel phase just below the phase transition is measure of the relative strength of the cross term. This might explain the experimental impression that the misalignment is small. This would mean that the exchange is mostly determined by the separate longitudinal and transverse terms.

Intuitively this makes sense since the presence of the mixed term is subtle effect having to do with the action of full crystal symmetries on the exchange. Note that this means that it does not appear if you were to analyze an isolated bond, but the largest exchange anisotropy can be expected from the geometry within each bond. That will tend to lock the Néel field to the strain direction.

So the conclusion is that a linear coupling to strain provides a director that can orient the Néel vector. Ignoring “cross coupling” of spin polarizations in each bond one would lock the favored Néel vector along a principal strain axis. Including it defines an intrinsic misorientation in the bilinear spin Hamiltonian. The previous Landau theory finds a competition between intrinsic sixfold lattice anisotropy and the direction determined by the strain. The lattice model says that the Néel field determined by the strain need not be exactly along a principal strain axis, but it would be in the absence of the cross coupling contributions to the exchange matrix.

-
- [1] Wiedenmann, A., Rossat-Mignod, J., Louisy, A., Brec, R. & Rouxel, J. Neutron diffraction study of the layered compounds MnPSe_3 and FePSe_3 . *Solid State Commun.* **40**, 1067–1072 (1981).
 - [2] Sa, D., Valenti, R. & Gros, C. A generalized Ginzburg-Landau approach to second harmonic generation. *Eur. Phys. J. B* **14**, 301–305 (2000).
 - [3] Grasso, V. & Silipigni, L. Optical absorption and reflectivity study of the layered MnPSe_3 seleniophosphate. *J. Opt. Soc. Am. B* **16**, 132–136 (1999).
 - [4] Wang, H. & Qian, X. Giant optical second harmonic generation in two-dimensional multiferroics. *Nano Lett.* **17**, 5027–5034 (2017). PMID: 28671472.
 - [5] Wang, H. & Qian, X. Ferroicity-driven nonlinear photocurrent switching in time-reversal invariant ferroic materials. *Sci. Adv.* **5** (2019).
 - [6] Liu, Z. *et al.* Strain and structure heterogeneity in MoS_2 atomic layers grown by chemical vapour deposition. *Nat. Commun.* **5**, 5246 (2014).
-